

# Air–Sea Interactions and Biogeochemical Responses to Medicane Daniel

Babita Jangir and Ehud Strobach

Institute of Soil, Water and Environmental Sciences, Volcani Institute, Agriculture Research Organization, Rishon LeTsiyon, Israel

\*Corresponding author: Babita Jangir (bj11@iitbbs.ac.in)

**Abstract:** Medicane Daniel, formed on 4-12 September 2023, stands out as the deadliest recorded storm in Mediterranean history. In this study, we investigate the role of sea features in the intensification of the medicane Daniel and the response of biogeochemical properties to the storm. Our results show that medicane Daniel intensified immediately prior to landfall in a coastal environment characterized by the co-occurrence of a warm-core eddy (WCE), elevated ocean heat content, and a moderate marine heatwave, highlighting (MHW), suggesting that sea anomalies may have supported or modulated the role of pre-existing upper-ocean thermal conditions in supporting its intensification under favorable atmospheric forcing. Additionally, observations from the high-resolution Surface Water and Ocean Topography (SWOT) satellite reveal a larger anticyclonic eddy than that depicted in lower-resolution products, thereby further supporting the hypothesis of sea-induced intensification. The favorable conditions at the sea before landfall enhanced were accompanied by moisture convergence and moisture supply in the atmosphere above, leading to intense precipitation in this region. Biogeochemical properties were strongly affected by cyclone-induced subsurface vertical mixing and upwelling. Focusing on two eddies in the vicinity of the maximum cyclone intensity, we found that the observed vertical displacement of the deep chlorophyll maximum exceeds that expected by direct wind-driven upwelling alone, suggesting additional contribution from a structural isopycnal adjustment triggered by the neutralization of eddy vorticity. We propose that the medicane destabilized destabilizes the eddies' internal balance, leading to a large-scale reorganization of the water column that persists longer in the WCE than the transient response observed in the cold-core eddy (CCE-).

**Key Words:** Medicanes, eddies, marine heatwave, medicane Daniel, SWOT satellite, Biogeochemistry biogeochemistry

**Key Points:**

- 34 ● Co-occurring warm-core eddies, marine heatwave, and elevated ocean heat content  
35 ~~created optimal conditions~~provided support for the rapid intensification of  
36 ~~Medicanemedicane~~ Daniel near landfall.
- 37 ● High-resolution SWOT observations ~~reveal~~indicate stronger and larger eddy structures  
38 than conventional datasets, ~~highlightingsupporting~~ their critical role in air–sea  
39 interactions.
- 40 ● Interaction with warm-core eddies amplifies vertical mixing and nutrient supply,  
41 leading to enhanced chlorophyll and productivity responses.
- 42 ● Cyclone-induced biogeochemical response is influenced by subsurface restructuring  
43 and isopycnal adjustment, exceeding expectations from Ekman-driven upwelling alone.
- 44 ● Results demonstrate that compound ocean extremes can significantly enhance both  
45 cyclone intensity and ocean biogeochemical impacts.

46

## 47 **1. Introduction:**

48 The Mediterranean region is recognized as a climate change hotspot (IPCC, 2021), warming at  
49 a rate up to 1.5 times faster than the global average (MedECC, 2020; Zittis et al., 2022;  
50 Khodayar et al., 2025). Situated between the arid climate of North Africa and the temperate  
51 and wet climate of Central Europe, the Mediterranean region is particularly vulnerable to future  
52 climate impacts. Surface temperature in this region is projected to continue increasing, but the  
53 precipitation tends to decrease (Cherif et al., 2020; Reale et al., 2022). As a consequence, the  
54 magnitude of extreme events such as Mediterranean cyclones, marine heatwaves (MHWs), and  
55 intense droughts is projected to increase under future climate scenarios (MedECC, 2020;  
56 Hochman et al., 2021; Zittis et al., 2022).

57

58 Medicanes are a subcategory of Mediterranean cyclones, which can resemble hurricanes in  
59 both intensity and impact. They often bring torrential rainfall, flash floods, powerful winds,  
60 storm surges, and hazardous sea conditions. Such events pose significant risks, particularly to  
61 coastal communities and urban centers, threatening homes, livelihoods, and natural ecosystems  
62 (Hochman et al., 2021; Khodayar et al., 2025). Similar to Mediterranean cyclones, medicane’s  
63 intensity is projected to increase under future climate scenarios, but with lower frequency

64 (González-Alemán et al., 2019). Despite their strong impact, the full extent of the damage  
65 medicanes inflict, both socially and economically, remains insufficiently understood.  
66 Moreover, their potential impact on ocean biogeochemistry is under-researched and often  
67 poorly communicated, leaving a critical gap in public awareness and scientific insight.

68

69 Medicanes are also known as ‘tropical-like cyclones’ because they have tropical cyclone-like  
70 characteristics such as a cloud-free calm "eye," spiralling cloud bands, and strong winds near  
71 the vortex centre. These features may be associated with the absence of fronts, weak vertical  
72 wind shear, and a warm-core with an axisymmetric structure (Miglietta et al., 2019; Flaounas  
73 et al., 2022; Panegrossi et al., 2023). The formation of cyclones in the Mediterranean region  
74 including medicanes, is primarily driven by baroclinic instability and Rossby wave breaking  
75 (Raveh-Rubin and Flaounas, 2017; Flaounas et al., 2022). As these systems evolve and reach  
76 their mature stage, medicanes can intensify and be sustained through exchanges of heat and  
77 momentum at the air-sea interface (Emanuel, 2005). The development of intense  
78 Mediterranean cyclones is frequently associated with southward shifts of the polar jet, which  
79 enable air masses with high potential vorticity to enter the Mediterranean region, thereby  
80 initiating baroclinic instability similar to that observed during extratropical cyclone  
81 development over open oceans (Flocas, 2000; Trigo et al., 2002; Nicolaidis et al., 2006; Fita  
82 et al., 2007; Claud et al., 2010; Kouroutzoglou et al., 2011; Flaounas et al., 2015). Raveh-Rubin  
83 and Flaounas (2017) identified Rossby wave breaking as a frequent precursor to Mediterranean  
84 cyclogenesis, while Flaounas et al. (2015) further emphasized that the cyclogenesis  
85 environment in the region is characterized by strong horizontal shear, driving these cyclones  
86 to follow a typical baroclinic life cycle. Furthermore, Flaounas et al. (2025) also highlight the  
87 importance of these atmospheric variables in the genesis and intensification of  
88 ~~Medicane~~medicane Daniel. In this manuscript, we primarily focus on potential atmospheric  
89 and oceanic precursors that are associated with Daniel’s intensification and ensuing  
90 precipitation.

91

92 Furthermore, the role of underlying ocean eddies and ~~marine heatwaves~~MHWs in modulating  
93 the deepening of a cyclone is often overlooked. Recent studies have highlighted the critical role  
94 of ocean eddies and MHWs in modulating cyclone’s deepening in the Mediterranean region  
95 (Jangir et al., 2023, 2024; Mishra et al., 2024; Strobach et al., 2024). In particular, Jangir et al.  
96 (2024) demonstrated the significant intensification of medicane Ianos due to the presence of a  
97 strong MHW, making it the only category 2 cyclone observed in the Mediterranean Sea. In

98 contrast, other medicanes such as Zorbas and Apollo intensified primarily due to the interaction  
99 with warm-core eddies (WCEs) along their paths. Mishra et al. (2024) reported that if we  
100 remove these Sea Surface Temperature (SST) anomalies from the path of medicane Ianos, the  
101 medicane will still form, but with a reduced intensity. Strobach et al. (2024) reported that ocean  
102 mesoscale eddies in the Eastern Mediterranean can significantly influence extreme weather, as  
103 shown during the heavy rainfall event in Israel that occurred from January 8 to 10, 2020. High-  
104 resolution coupled ocean-atmosphere simulations captured the event more accurately than  
105 uncoupled ones. The study by Strobach et al. (2024) highlights how eddies can enhance  
106 atmospheric moisture and meso-cyclone development, intensifying local extremes.

107

108 As efforts continue to enhance the accuracy of cyclone intensity forecasts, the potential  
109 influence of eddies, ~~marine heatwaves~~MHWs, and ocean heat content (OHC) remains a critical  
110 yet less explored aspect, particularly within the Mediterranean context. To improve the  
111 prediction of Mediterranean cyclones and mitigate associated risks, a deeper understanding of  
112 air-sea interaction processes, specifically surface heat fluxes, momentum fluxes, and upper-  
113 ocean thermodynamic responses, and the role of pre-existing oceanic conditions in cyclone  
114 genesis and intensification, is essential. Recent studies have increasingly focused on these  
115 dynamics, exploring how air-sea exchanges affect not only medicanes intensity but also the  
116 ocean's biogeochemical responses (Jangir et al., 2023; Menna et al., 2023; Scardino et al., 2024;  
117 Avolio et al., 2024). Notably, Jangir et al. (2023) highlighted the influence of WCEs on the  
118 intensification of medicanes, demonstrating that eddy size also plays a critical role; larger  
119 eddies tend to promote stronger cyclones and heavier rainfall. In this particular study, we show  
120 the influence of eddies and ~~marine heatwave~~MHW on the intensity of medicane Daniel.

121

122 Most of the studies use the satellite sea level anomaly (SLA) altimetry data from the Copernicus  
123 Marine Services (CMEMS) for the detection of eddies. Here, we also use the Surface Water  
124 and Ocean Topography (SWOT) satellite data, which are available at high spatial resolution.  
125 The SWOT satellite provides the first-ever global observations of ocean dynamics at sub-  
126 mesoscale spatial resolutions (1–100 km). While traditional satellite products, such as those  
127 from the Copernicus mission, offer spatial resolutions of approximately 25 km globally and  
128 12.5 km in the Mediterranean Sea, SWOT's advanced wide-swath altimetry overcomes these  
129 limitations by achieving resolutions as fine as 250 m to 2 km. This enhanced capability enables  
130 the detection of small-scale ocean features that were previously ~~unresolved~~misrepresented.  
131 SWOT observations confirm the widespread presence of sub-mesoscale eddies and internal

132 waves, particularly energetic in regions like western boundary currents and the Antarctic  
133 Circumpolar Current (Archer et al., 2025; Tranchant et al., 2025). This high-resolution data is  
134 especially valuable for studying ocean-atmosphere interactions, such as the role of eddies in  
135 cyclone intensification. In particular, SWOT's ability to capture the structure, intensity, and  
136 evolution of eddies provides critical insight into how these features influence heat transport,  
137 vertical mixing, and the modulation of cyclone intensity due to eddies. Thus, SWOT marks a  
138 transformative step in advancing our understanding of fine-scale ocean processes and their  
139 implications for weather, climate, and marine biogeochemistry.

140

141 Atmospheric cyclones are known to trigger substantial phytoplankton blooms (Shang et al.,  
142 2015; Chowdhury et al., 2020; Liu et al., 2020). These blooms are primarily attributed to  
143 cyclone-induced upwelling and vertical mixing, which transport cold, nutrient-rich, or  
144 chlorophyll-loaded water into the euphotic zone, stimulating phytoplankton bloom. Such  
145 storm-driven biological responses offer valuable insight into ocean mixing and biogeochemical  
146 dynamics (Chen et al., 2022). Additionally, strong cyclonic winds often cause a noticeable  
147 decrease in SST, which plays a crucial role in regulating primary productivity (Latha et al.,  
148 2015). There are a few studies reported in the other ocean basins that indicate the enhancement  
149 of chlorophyll a (Chl-a) concentration following the passage of a cyclone in the presence of  
150 eddies (Dutta et al., 2019; Zhang and Qui, 2020; Vidya et al., 2021) and ~~marine heatwave~~MHW  
151 (Oliver et al., 2018; Jangir et al., 2024). Recently, a study by Scardino et al. (2025) reported  
152 the response of Mediterranean cyclones on ocean chlorophyll concentration, primarily using  
153 Bio-Argo floats. In contrast, our study offers a new perspective by utilizing subsurface profiles  
154 of a broader suite of biogeochemical variables, including chlorophyll, phytoplankton, nutrients,  
155 and oxygen concentration, complemented by multiple ocean satellite and reanalysis products.  
156 To date, such a comprehensive assessment has rarely been reported for the Mediterranean Sea.  
157 Here, we investigate the impact of medicane Daniel on ocean biogeochemistry in the context  
158 of the SST anomalies along its path.

159

160 In this study, we highlight the co-occurrence of compound extreme events in the region prior  
161 to medicane Daniel's landfall. Specifically, we show that the intensification of medicane Daniel  
162 may have been driven by the combined influence of a WCE and ~~a marine heatwave~~an MHW.  
163 We examine the key atmospheric and oceanic factors that contributed to Daniel's development.  
164 The analysis also highlights the unique perspective offered by the SWOT satellite, capturing  
165 aspects of air-sea interaction that traditional datasets do not resolve. Additionally, we

166 investigate the medicane's impact on ocean biogeochemistry along its path, and specifically at  
167 the WCE location prior to landfall, providing insights into the underlying physical and  
168 biological processes that govern such interactions.

169

170 **2. Synoptic evolution and impacts of medicane Daniel:** On September 2-3, a swift cold front  
171 traversed Central Europe, generating an upper-level trough that created a cut-off low near  
172 Greece by September 4. Named "Daniel" by the Hellenic National Weather Service, this  
173 cyclone brought severe thunderstorms to Greece, Turkey, and Bulgaria due to unstable  
174 atmospheric conditions and warm waters. Daniel traversed the Mediterranean Sea from 4 to 12  
175 September 2023, bringing exceptionally heavy rainfall to Greece and Libya and triggering  
176 severe floods and mudslides. While moving south-southwest, Daniel stalled over the central  
177 Mediterranean, evolving into a subtropical storm by September 7. By September 9, Daniel  
178 transitioned into a tropical-like storm, making landfall in Libya on September 10. Daniel  
179 dissipated into a low-pressure trough by September 12 (Hérincs, 2023; Normand et al., 2024).  
180 Medicane Daniel brought intense winds of up to 120 km/h and delivered a total of 240 mm of  
181 rainfall over 25 hours (Normand et al., 2024). It caused catastrophic flash flooding in Derna on  
182 September 10, 2023, as torrential rains overwhelmed the river's delta outlet. The flood  
183 destroyed large parts of the city's buildings, infrastructure, and bridges, resulting in 8.8 million  
184 tons of debris. In Derna alone, 10% of houses were destroyed and 18.5% damaged. In other  
185 cities, such as Susah, approximately 28% of homes were destroyed, while Albayda, Al-Marj,  
186 and others also suffered heavy losses. Overall, the storm led to 5,898 deaths, 8,000 missing  
187 persons, 44,800 displaced individuals, and 18,838 homes damaged across Libya's northeastern  
188 coast, making it the deadliest African storm since 1900 (Hérincs, 2023; Normand et al., 2024;  
189 Katsanos et al., 2024).

190

### 191 **3. Data and Methods:**

#### 192 **3.1 Data sources and products used:**

193 In this study, the best-track data for the medicane Daniel was obtained from the Zivipotty  
194 Cyclone Report database (<https://zivipotty.hu/tcr.html>). Eddy identification was based on daily  
195 SLA fields sourced from the CMEMS. Specifically, the dataset  
196 SEALEVEL\_EUR\_PHY\_L4\_NRT\_OBSERVATIONS\_008\_060, with a spatial resolution of  
197 0.125°, was utilized. To detect and characterize the ~~marine heatwave~~MHW, daily SST data  
198 from the NOAA Optimum Interpolation SST V2 dataset (Reynolds et al., 2007) were used.  
199 This dataset has a spatial resolution of 0.25° and covers the period from 1981 to the present.

200 The key atmospheric variables, including total column water (which represents the sum of  
 201 water vapor, liquid water, cloud ice, rain, and snow in a column extending from the surface of  
 202 the Earth to the top of the atmosphere), total precipitation, vertically integrated moisture  
 203 divergence, mean sea level pressure (MSLP), 10-meter zonal and meridional wind components,  
 204 daily radiative fluxes of shortwave and longwave radiations, (denoted as  $Q_{SW}$  and  $Q_{LW}$   
 205 respectively), and turbulent heat fluxes of latent and sensible flux (denoted as  $Q_{lat}$  and  $Q_{sen}$   
 206 respectively) were retrieved from the ERA5 reanalysis (Hersbach et al., 2020). The surface net  
 207 heat flux ( $Q_{net}$ ) was derived from a combination of radiative and turbulent fluxes (Menna et al.,  
 208 2023).

$$209 \quad Q_{net} = Q_{SW} - Q_{LW} - Q_{lat} - Q_{sen} \dots\dots\dots(1)$$

211 High-resolution SLA observations were obtained from the SWOT Level 3 satellite product,  
 212 which offers 2 km spatial resolution, provided by Archiving, Validation and Interpretation of  
 213 Satellite Oceanographic data (AVISO; [https://www.aviso.altimetry.fr/en/data/products/sea-](https://www.aviso.altimetry.fr/en/data/products/sea-surface-height-products/global/swot-l3-ocean-products.html)  
 214 [surface-height-products/global/swot-l3-ocean-products.html](https://www.aviso.altimetry.fr/en/data/products/sea-surface-height-products/global/swot-l3-ocean-products.html)).

215 Lastly, biogeochemical variables such as chlorophyll, phytoplankton, nutrients, and dissolved  
 216 oxygen were accessed via the CMEMS from the product  
 217 [MEDSEA\\_MULTIYEAR\\_BGC\\_006\\_008](https://doi.org/10.25423/cmcc/medsea_multiyear_bgc_006_008), available at a 4-5 km spatial resolution, and 1-hr  
 218 temporal resolution (   
 219 [https://doi.org/10.25423/cmcc/medsea\\_multiyear\\_bgc\\_006\\_008\\_medbfm3](https://doi.org/10.25423/cmcc/medsea_multiyear_bgc_006_008_medbfm3)). Daily satellite-  
 220 derived chlorophyll products (OCEANCOLOUR\_MED\_BGC\_L4\_NRT) with a spatial  
 221 resolution of 1 km were used in this study (Volpe et al., 2019; Volpe et al., 2018; Berthon and  
 222 Zibordi, 2004). These datasets are archived by the Copernicus Marine Service  
 223 (<https://doi.org/10.48670/moi-00298>) and are provided by the Italian National Research  
 224 Council (CNR, Rome, Italy), with data availability from January 2023 to the present. The  
 225 multi-sensor product integrates observations from SeaWiFS, MODIS, MERIS, VIIRS, and  
 226 OLCI, and includes key biogeochemical variables such as chlorophyll-a (Chl-a), diffuse  
 227 attenuation coefficient at 490 nm, and primary production.

228 Despite their advantages, these datasets are subject to uncertainties arising from atmospheric  
 229 correction errors, cloud contamination, aerosol effects, and reduced accuracy in optically  
 230 complex coastal waters. In addition, the gap-filling procedure used to generate continuous  
 231 fields may introduce smoothing in regions with persistent data gaps. Nevertheless, these

232 products provide robust, high-resolution information on surface biogeochemical variability  
233 associated with cyclone-induced ocean processes.

234 **3.2 Methods:** In this study, we investigate the intensification, structure, and impacts of  
235 medicane Daniel. This section outlines the methodologies used to analyze the oceanic and  
236 atmospheric conditions associated with the event. The analysis focuses on key processes  
237 influencing cyclone formation and intensification, including the role of oceanic features such  
238 as WCEs and ~~marine heatwaves~~MHWs, the contribution of ocean heat content as a source of  
239 subsurface thermal energy, and atmospheric variables such as moisture and wind fields. The  
240 methods used for the identification of the sea eddies and MHWs, as well as the computation of  
241 ocean heat content, are described below.

242

### 243 **3.2.1 Eddy and marine heatwave identification:**

244 Eddy identification in this study followed the approach of Jangir et al. (2021, 2023) and Sun et  
245 al. (2017), based on geostrophic balance equations relating SLA to geostrophic currents. zonal  
246 ( $u$ ) and meridional ( $v$ ) velocity components were derived using equations 2, 3, and 4:

$$247 \quad u = -\frac{g}{f} \left( \frac{dh}{dy} \right) \dots \dots \dots (2)$$

$$248 \quad v = \frac{g}{f} \left( \frac{dh}{dx} \right) \dots \dots \dots (3)$$

$$249 \quad V^2 = u^2 + v^2 \dots \dots \dots (4)$$

250

251 where  $g$  is the acceleration caused by gravity,  $f$  is the Coriolis parameter,  $h$  is the SLA, and  $V$  is  
252 the geostrophic current speed.

253

254 Eddies were classified by analysing flow circulation and SLA patterns: anti-cyclonic  
255 circulation with a local SLA maximum indicated a WCE, while cyclonic circulation with a  
256 local SLA minimum indicated a cold-core eddy (CCE). This is consistent with previous  
257 findings, where WCEs in the Northern hemisphere exhibited clockwise (anti-cyclonic)  
258 rotation, while CCEs rotated counterclockwise (cyclonic). The relation between anti-cyclonic  
259 eddies and WCEs along the cyclone's path was also verified by inspecting SST anomalies with  
260 respect to a boxcar average.

261

262 MHWs were identified using the definition by Hobday et al. (2016) and the software developed  
263 by Zhao et al. (2019) ([https://github.com/ZijieZhaoMMHW/m\\_mhw1.0](https://github.com/ZijieZhaoMMHW/m_mhw1.0)). An MHW is defined

264 as a period of at least five consecutive days during which the daily SST exceeds the seasonally  
 265 varying 90<sup>th</sup> percentile, based on a climatological reference period (1983–2021). Events  
 266 separated by less than three days are treated as a single MHW. Daily SST anomalies were  
 267 computed by subtracting the daily climatology. MHW intensity was classified following  
 268 Hobday et al. (2018) into four categories based on the metric  $\theta$ , where  $\theta$  represents the  
 269 normalized SST anomaly relative to the climatological threshold. It is defined as:

270 
$$\theta = \frac{SST - SST_{climatology}}{SST_{90th\ percentile} - SST_{climatology}} \dots\dots\dots(5)$$

271 where SST is the daily sea surface temperature,  $SST_{climatology}$  is the climatological mean SST,  
 272 and  $SST_{90th\ percentile}$  is the seasonally varying 90<sup>th</sup> percentile threshold. Based on this metric,  
 273 MHW intensity is categorized as follows: moderate ( $1 \leq \theta \leq 2$ ), strong ( $2 \leq \theta \leq 3$ ), severe ( $3 \leq$   
 274  $\theta \leq 4$ ), and extreme ( $\theta \geq 4$ ).

275 **3.2.2 Computation of ocean heat content**

276 We have also calculated the OHC to assess the role of subsurface heat accumulation in driving  
 277 compound extreme events, such as the co-occurrence of MHWs and cyclones. Since the ocean  
 278 acts as a key energy source for cyclones by supplying heat and moisture, the passage of a  
 279 cyclone typically extracts heat from the upper ocean, leading to a decrease in OHC. In this  
 280 study, OHC is defined as the vertically integrated thermal energy from the surface down to the  
 281 depth of the 20 °C isotherm (a proxy for the thermocline layer). The OHC was computed for  
 282 the medicane using the following formulation (Equation 6):

283 
$$OHC = \int_{h1}^{h2} \rho C_p T dz \dots\dots\dots(6)$$

284 where  $\rho$  is the density of the seawater,  $C_p$  is the specific heat capacity of the seawater at  
 285 constant pressure,  $p$ ,  $h1$  is the surface,  $h2$  is the bottom depth, and  $T$  is the temperature in °C.  
 286 This approach allows us to quantify how much thermal energy is available in the upper ocean  
 287 to potentially intensify cyclones and how this energy is depleted following cyclone passage.

288 **3.2.3 Computation of Ekman pumping**

289 Ekman pumping was computed using the wind stress components  $\tau=(\tau_x, \tau_y)$  from ERA5,  
 290 namely Eastward Wind Stress (EWSS) and Northward Wind Stress (NSSS), which is available

291 for  $0.25^\circ \times 0.25^\circ$  and hourly temporal resolution. To compute the wind stress curl ( $\nabla \times \tau$ ), the  
 292 spatial derivatives of wind stress are used, and it is computed using equation 7:

293

$$294 \quad curl(\tau) = \frac{\partial \tau_y}{\partial x} - \frac{\partial \tau_x}{\partial y} \dots\dots\dots(7)$$

295

296 The wind stress curl ( $\nabla \times \tau$ ) was calculated using finite-difference estimates of spatial gradients  
 297 on a latitude-longitude grid, with grid spacing converted to metric units. No additional  
 298 smoothing was applied to the wind stress fields prior to curl computation. Then, the Ekman  
 299 pumping velocity ( $w_e$ ), introduced by Stern (1965) to account for the effect of the ocean  
 300 currents on upwelling, is calculated using equation 8:

301

$$302 \quad w_e = \frac{1}{\rho} \times curl\left(\frac{\tau}{f+\zeta}\right) \dots\dots\dots(8)$$

303

304 This vertical velocity reflects the upwelling (positive  $w_e$ ) or downwelling (negative  $w_e$ ) of  
 305 water, and is a crucial mechanism through which cyclones influence oceanic nutrient transport,  
 306 mixing, and biological productivity (Li et al., 2021). Here, the relative vorticity ( $\zeta$ ) was  
 307 computed from the zonal ( $u$ ) and meridional ( $v$ ) components of the surface current, as given in  
 308 Equation (9):

309

$$\zeta = \frac{\partial v}{\partial x} - \frac{\partial u}{\partial y} \dots\dots\dots(9)$$

310

311 The Ekman transport vector components were computed from the wind stress and Coriolis  
 312 parameter as:

313

$$M_x = \frac{\tau_y}{\rho(f+\zeta)} \dots\dots\dots(10)$$

314

$$M_y = \frac{\tau_x}{\rho(f+\zeta)} \dots\dots\dots(11)$$

315

316 where  $\rho$  is seawater density, and  $f$  is the Coriolis parameter (dependent on latitude). The vector  
 317 field  $M=(M_x, M_y)$  was visualized using quiver plots to reveal the spatial structure and  
 318 directional response of Ekman transport to cyclone wind forcing.

319

320 **3.2.4 Computation of various properties along the track of medicane Daniel**

321 To estimate the medicane's characteristic MSLP and wind speed along the cyclone track, we  
322 applied Cressman averaging (Cressman, 1959). Once the cyclone center was identified, a  
323 spatial average within a 2° radius around the center, weighted by inverse square distance, was  
324 computed for MSLP and wind speed. This method captures changes within a 2-degree radius  
325 of the cyclone centre, while regions outside this radius are not included. Similarly, daily MHW  
326 and high-pass filtered (500 km radius) SST and OHC anomalies, along with their along-track  
327 evolution during ~~Cyclone~~medicane Daniel ~~where, were~~ calculated using the 2-degree search  
328 radius and the Cressman interpolation technique. This analysis allows quantification of the  
329 relative extremity of the oceanic conditions encountered during intensification. The approach  
330 was used to assess variations in cyclone intensity along its path and has been widely employed  
331 in previous studies (Jangir et al., 2023).

332

#### 333 **4. Results and discussion**

334 In this section, we present the results of our study on medicane Daniel, focusing on two primary  
335 aspects. First, we analyze the influence of pre-existing oceanic conditions, specifically WCEs  
336 and MHW conditions, on the cyclone's intensification. Second, we investigate the medicane's  
337 impact on ocean biogeochemistry, particularly the observed increase in surface productivity as  
338 indicated by enhanced biogeochemical variables. Our findings also explore the physical  
339 mechanisms behind these changes, highlighting the interactions between the ocean and  
340 atmosphere throughout the lifecycle of medicane Daniel.

##### 341 *4.1 Role of oceanic features in intensification of medicane Daniel*

342 Figure 1a-b shows the SLA along the medicane's track. At first, the medicane passed over a  
343 cluster of three anticyclonic eddies between September 4 and 6, presumably contributing to its  
344 intensification (Jangir et al., 2023). This intensification between 8 and 10 September was also  
345 supported by the presence of a moderate MHW, as shown in Figure 1c–e (see also SI Figure  
346 1). Furthermore, just before making landfall, the medicane arrived in a region characterized  
347 mostly by anticyclonic mesoscale WCE activity (figure 1f–h). OHC anomaly shown in Figure  
348 1i–k indicates higher heat content in the southern part of the domain close to landfall location,  
349 also supporting the intensification of the medicane. In addition to the maps in panels c–k of  
350 Figure 1, the analysis was carried out by computing MHW, SST, and OHC anomalies at each  
351 6-hourly track position (Figure 1l–n), with particular emphasis on the maximum cyclone  
352 intensity (Max-CI) location. We observed from the analysis that the maximal values of MHW;

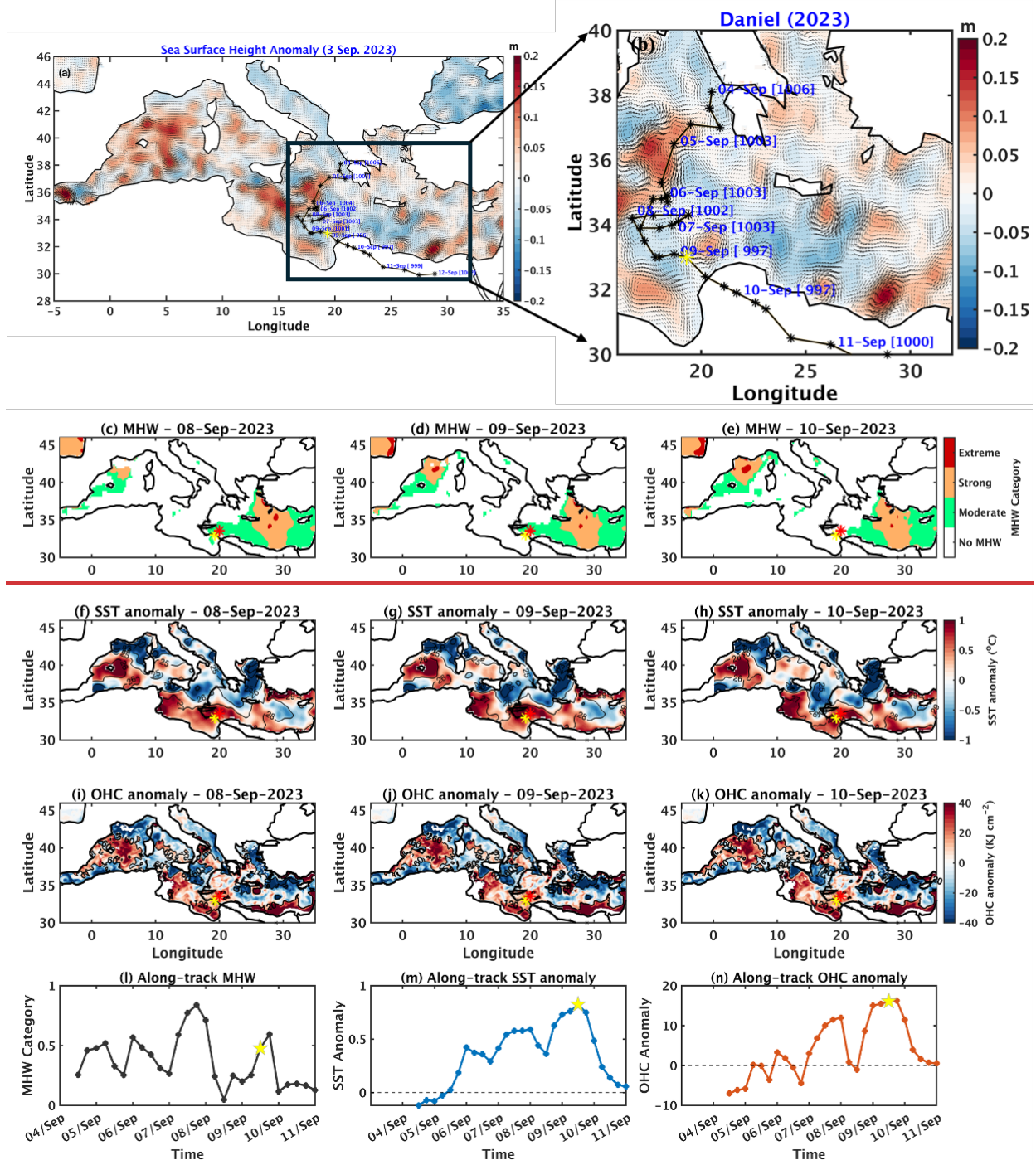
353 (~0.6), SST<sub>7</sub> (~0.83 °C), and OHC (~ 16.30 KJ/cm<sup>2</sup>) anomalies occurred in the last two days  
354 before Max-CI, indicating that medicane Daniel intensified over thermodynamically  
355 favourable conditions that were among the most anomalous along its track.

356 The combination of two extreme oceanic preconditions, namely the WCE and the MHW,  
357 together with high absolute values of OHC at the intensification site near the coastal region,  
358 may have contributed to the deadly outcome of this medicane. Rathore et al. (2022) and Jangir  
359 et al. (2024) highlighted the critical role of sudden intensification in Cyclone Amphan over the  
360 Indian Ocean and medicane Ianos over the Mediterranean Sea, respectively, in the presence of  
361 MHWs along their paths. The findings of the current study are consistent with these  
362 observations, demonstrating that while cyclone genesis and intensification can occur  
363 independently of such features, the presence of WCEs and MHWs may enhance the rate and  
364 magnitude of intensification over a shorter time.

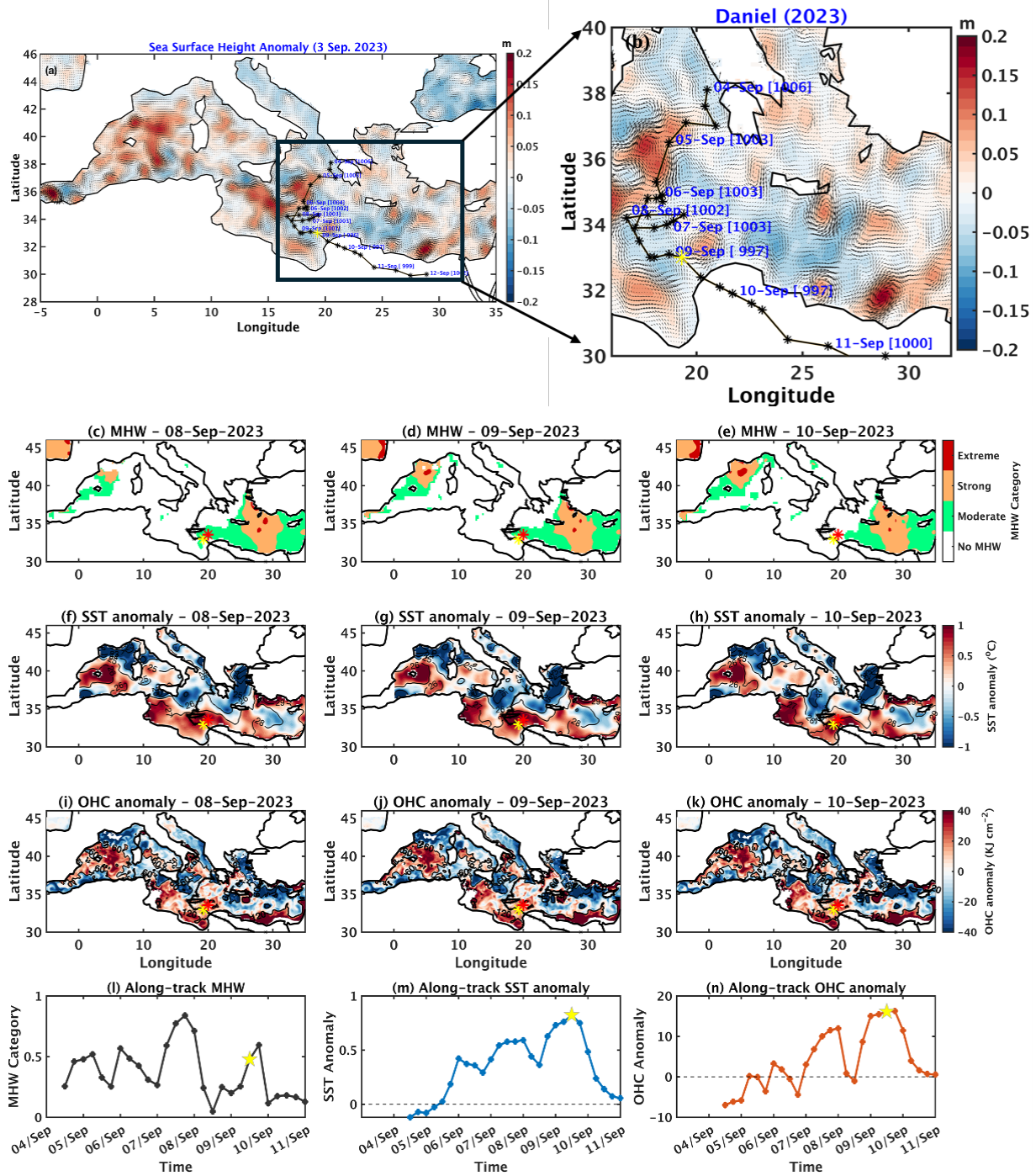
365 Figure 1 also highlights the potential importance of ocean characteristics such as WCEs and  
366 MHWs in cyclone intensification, indicating that cyclone intensity increased in the presence of  
367 WCEs and MHWs. This behavior is similar to how cyclones in other ocean basins react to  
368 changes in intensification factors related to underlying eddies (Ali et al., 2007; Lin et al., 2013;  
369 Jangir et al., 2020; Jangir et al., 2023). When a cyclone encounters a WCE, the negative  
370 feedback loop between cyclone intensity and SST diminishes. Normally, cyclones extract heat  
371 from the ocean, resulting in surface cooling due to enhanced mixing and evaporation, which  
372 acts to reduce cyclone intensity. However, if a WCE or ~~marine heatwaves~~ MHWs are present,  
373 the high SST persists longer, intensifying the cyclone and reducing the negative feedback effect  
374 (Bender et al., 1993; Jangir et al., 2024).

375 Furthermore, atmospheric cyclones draw a significant portion of their energy from warm, deep  
376 ocean waters; therefore, quantifying the amount of this warm, deep water provides a more  
377 accurate measure of the energy available to the storm. OHC serves as this metric, indicating  
378 how much warm water a cyclone can convert into energy. Studies have shown that OHC is a  
379 far superior predictor compared to SST alone (Wada & Usui, 2007; Sharma and Ali, 2014; Lin  
380 et al., 2013; Law et al., 2011). Analysis of the OHC revealed a significant amount of OHC at  
381 the intensification locations, providing ~~the energy necessary~~ a favorable upper-ocean thermal  
382 reservoir for medicane Daniel to intensify. Approximately 120 KJ/cm<sup>2</sup> of heat was available  
383 from September 4<sup>th</sup> to 9<sup>th</sup>, even before the cyclone's intensification (Figure 1i-k & SI Figure 2).

384 This accumulated heat at the intensification location is attributed to the presence of the ~~warm-~~  
 385 ~~core eddy~~WCE and the ~~marine heatwave~~MHW, which decreases after the passage of the  
 386 medicane on the 11<sup>th</sup> and 12<sup>th</sup> of September, 2023 (SI Figure 2). The presence of heat in the  
 387 form of SST anomaly (Figure 1f-h) and OHC anomaly (Figure 1i-k) along the path of medicane  
 388 maintains intensity by reducing negative feedback that occurs due to the passage of the cyclone  
 389 (Jangir et al., 2023; Jangir et al., 2024).



390



391

392 *Figure 1: (a, b) Sea level anomaly (shading) with geostrophic currents (arrows). The medicane*  
 393 *track is overlaid on (c-e) marine heatwave (MHW), (f-h) sea surface temperature (SST)*  
 394 *anomalies (500 km radius high pass filter), and (i-k) ocean heat content (OHC) anomalies (500*  
 395 *km radius high pass filter). In panels f-k, absolute values are indicated by contours. Panels (l-*  
 396 *n) show along-track values of MHW, SST, and OHC anomalies. The yellow stars (pentagon)*  
 397 *in panels a-k (l-n) mark the location of maximum cyclone intensity (Max-CI), while the red*  
 398 *pentagons mark the Max-CI location defined by the minimum mean sea level pressure. The red*

399 *star marker in panels c-k indicates the position of the WCE. Dates for each panel are shown*  
400 *along the track.*

401

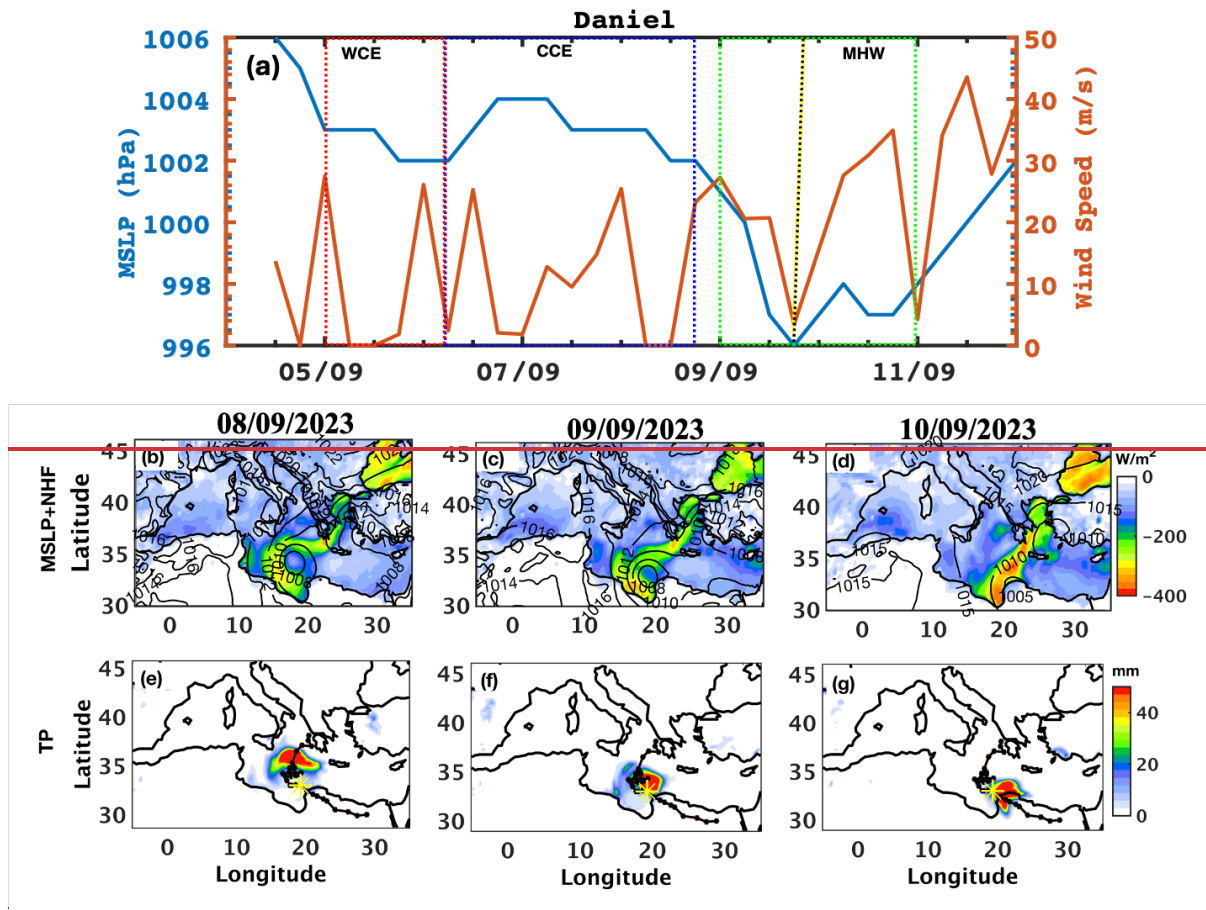
#### 402 ***4.2 The role of atmospheric precursors in the intensification of medicane Daniel***

403 The MSLP and wind speed, computed using the Cressman averaging method (Cressman, 1959)  
404 along the cyclone's track, are shown in Figure 2a. The MSLP indicates moderate intensification  
405 ~~for~~from 1006 hPa to 1002 hPa when the storm passes over the WCE on 5 September 2023  
406 (Figure 2a). Subsequently, from the 6th to the 7th September 2023, the medicane passes over  
407 a CCE region, and its intensity is reduced to 1004 hPa. Upon reaching the vicinity of Libya's  
408 coast on 8 September 2023, it quickly intensified. An additional WCE was present in the  
409 vicinity of the cyclone's path at that time, potentially further contributing to its fast  
410 intensification. This fast intensification is indicated by a drop in the MSLP and a sudden  
411 increase in wind speed near the eddy and MHW location (Figure 2a). The cutoff low, which  
412 was supported by high net heat flux, persisted for two days (Figures 2b-d, SI Figure 3), even  
413 after the cyclone made landfall in Libya.

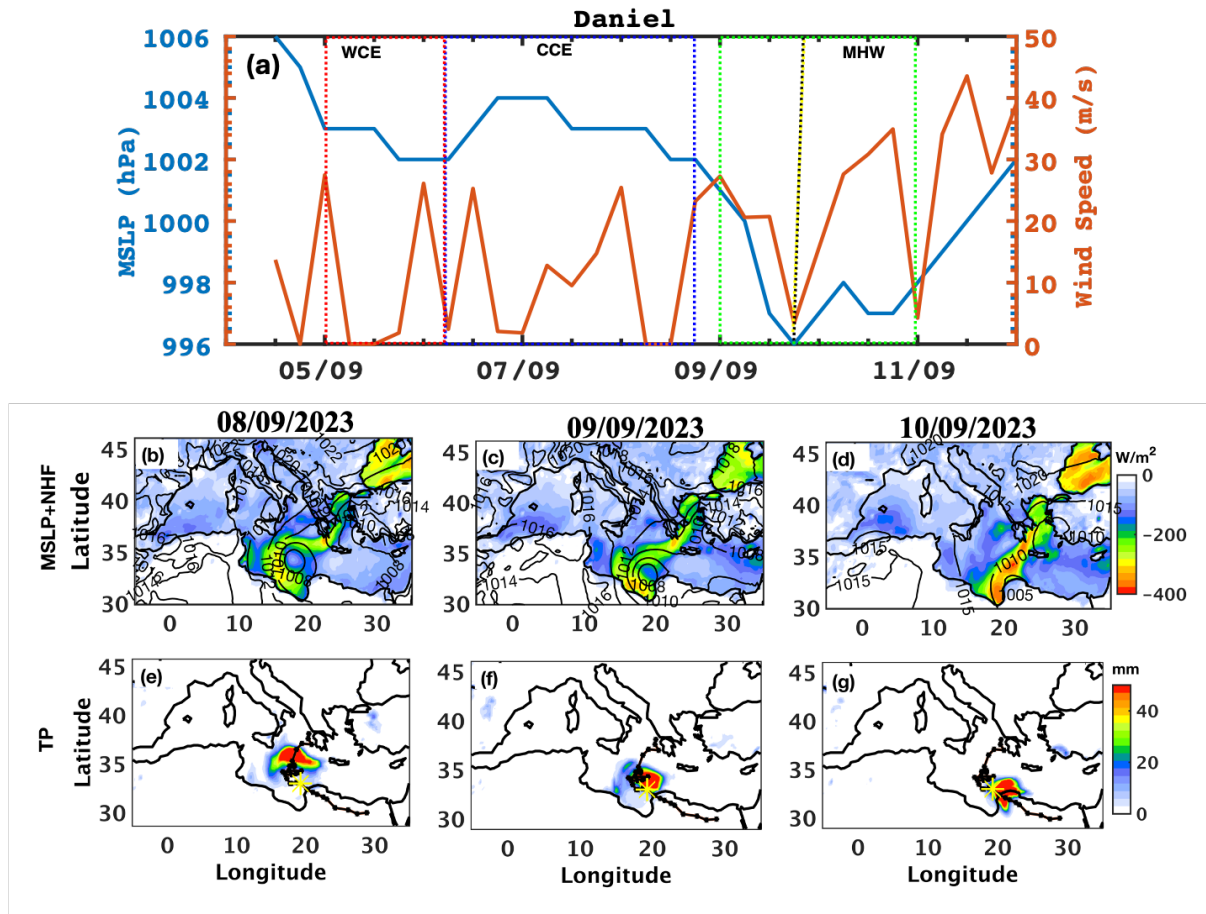
414 Moisture processes play an equally important role in cyclone intensification. Their importances  
415 been demonstrated in previous studies by Jangir et al. (2023) and Pytharoulis et al. (2018),  
416 emphasizing that elevated SST in the form of WCE or MHW is essential for providing moisture  
417 to a medicane via surface fluxes, enhancing convection. Additionally, Jangir et al. (2024)  
418 highlighted the importance of moisture convergence in the intensification of cyclones and  
419 increasing total associated precipitation. Thus, motivated by these findings, we focus in this  
420 study on the causes of the intensification of the medicane Daniel and the extreme flood that  
421 occurred during the event.

422 The analysis of moisture convergence (i.e., mean vertically integrated moisture divergence)  
423 showed a pattern of moisture convergence along the cyclone's path. Notably, this convergence  
424 coincides with the eddy location at the intensification location on September 9th, 2023 (SI  
425 Figure 4). This alignment suggests that the eddy supplied the moisture needed for the cyclone's  
426 intensification. The interaction between the eddy and the medicane likely enhanced moisture  
427 availability, contributing to the storm's strengthening at that specific point in its path.  
428 Additionally, the total column water was notably high at the WCE and MHW locations. While  
429 this total water was present before the intensification location as well, it converged around the  
430 eddy at the intensification location (SI Figure 5), leading to substantial precipitation in that area

431 (Figure 2e-g and SI Figure 6). The severe precipitation near the coastal region highly coincides  
 432 with the WCE and MHW. The WCE's influence intensified the cyclone by providing additional  
 433 moisture and heat, leading to heavy rainfall. This heavy precipitation, concentrated near the  
 434 coast, exacerbated the storm's impact, severely damaging the affected areas.



435



436  
 437 *Figure 2: (a) Mean sea level pressure (MSLP), and wind speed computed using the Cressman*  
 438 *average along the track of the medicane Daniel. The red, blue, and green boxes indicate the*  
 439 *locations of the warm-core eddy- (WCE), cold-core eddy (CCE) and marine heatwave- (MHW),*  
 440 *respectively. The medicane track is overlaid on (b-d) the daily mean of MSLP (contours) net*  
 441 *heat fluxes (shading; positive downward), and on (e-g) total precipitation for 8-10 September*  
 442 *2023. The yellow star indicates the location of maximum intensification (Max-CI).*

443

#### 444 **4.3 SWOT satellite data**

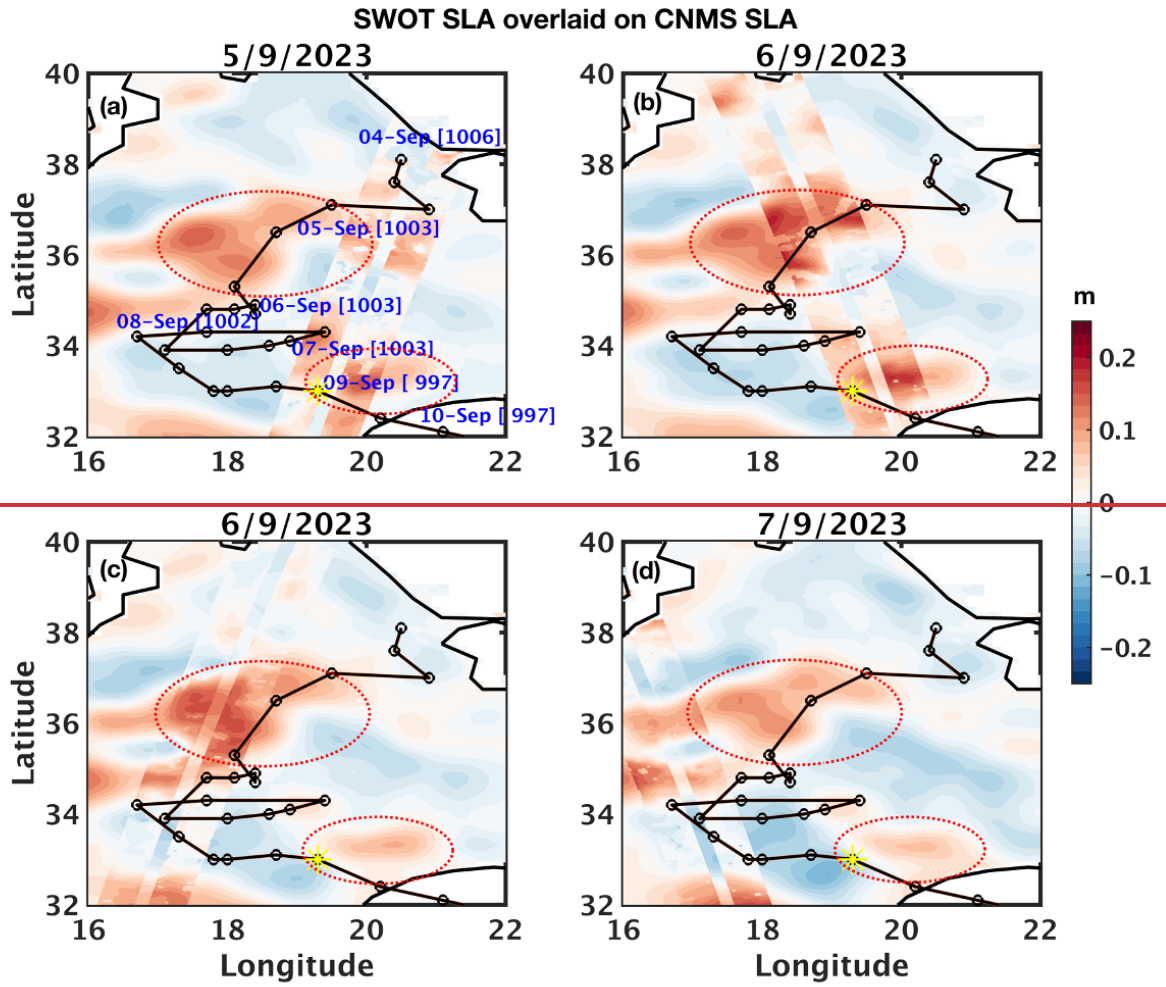
445 The SWOT mission offers high-resolution sea surface height anomaly (SSHA) or SLA data  
 446 with unprecedented spatial detail, enabling precise detection of mesoscale and sub-mesoscale  
 447 ocean features, such as eddies and fronts (Morrow et al., 2019). This can be valuable for  
 448 studying cyclones, which interact strongly with oceanic eddies that influence storm intensity.  
 449 Unlike traditional altimeters, SWOT's wide-swath coverage enables improved detection of  
 450 mesoscale and sub-mesoscale eddies, frontal gradients, and filaments that regulate ocean heat  
 451 distribution and air-sea exchanges. These features are often underrepresented in low-resolution  
 452 datasets, limiting their ability to capture localized processes such as eddy-cyclone interactions

453 and cyclone-induced mixing. ~~By resolving~~By improving the detection of these fine-scale  
454 physical structures, SWOT also provides a framework for interpreting biogeochemical  
455 responses. While coarse datasets show bulk chlorophyll changes, SWOT helps identify  
456 localized regions of enhanced mixing and upwelling that drive nutrient supply and biological  
457 variability. This allows for a clearer linkage between physical forcing and biogeochemical  
458 response. Overall, SWOT overcomes key limitations of conventional altimetry by preserving  
459 high-frequency spatial gradients, enabling a more accurate representation of the ocean state  
460 during extreme events such as medicane Daniel.

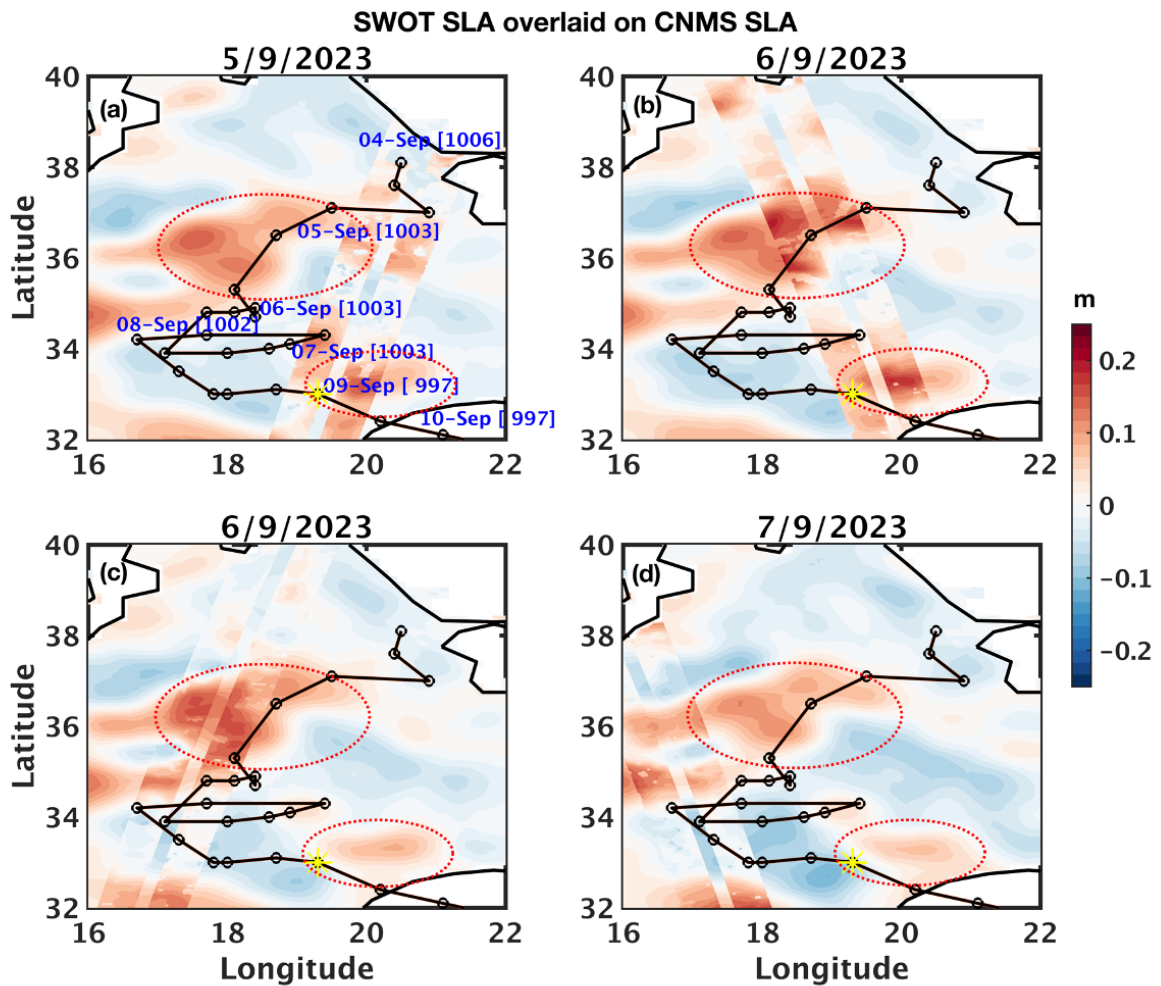
461

462 Here we show the SWOT swath passing over the location of the eddies along the track of  
463 medicane Daniel (Figure 3). In Figures 3a-b, the eddy initially appears small and low intensity  
464 in the CMEMS, and the cyclone is observed nearby. However, SWOT data reveal a more  
465 intense and extensive eddy structure than CMEMS, with the cyclone positioned directly above  
466 it. These findings report the value of SWOT observations in capturing fine-scale oceanic  
467 features and dynamics, offering critical insights into cyclone-eddy interactions.

468



469



470

471 *Figure 3: (a-d) The SWOT sea level anomaly (SLA) swath (2 km resolution) overlaid on SLA*  
 472 *from CMEMS (12.5 km spatial resolution). The dates shown above each panel correspond to*  
 473 *the periods of SWOT swath data availability.*

474

#### 475 **4.4 Impact of medicane Daniel on ocean biogeochemistry**

476 To investigate the impact of the medicane on oceanic physical (temperature and salinity) and  
 477 biogeochemical properties (i.e., chlorophyll-a, phytoplankton, nitrate and phosphate, and  
 478 oxygen concentration), we analyzed vertical profiles of key variables along the cyclone's track.

479 The analysis focused on differences between two days after the cyclone's passage, minus two  
 480 days before (Figure 4a-g). The results reveal a notable decrease in temperature along the

481 cyclone path, with a general strong cooling along its path except for a short pause in the cold  
 482 SST anomaly region in the morning of the 8th (Figure 1n). This region was also relatively

483 outside the MHW domain (Figure 1l). The salinity also decreases on the surface presumably  
 484 due to a massive influx of freshwater from heavy rainfall, again, except for the morning of the

485 8th, in which the cyclone was outside the influence of ~~warm-core eddies~~ WCEs and ~~marine~~  
 486 ~~heatwave~~ MHW (Figure 4b). In contrast, at the subsurface, Chl-a and phytoplankton

487 concentrations exhibit a marked dipole (Figure 4c-d), while nutrients increase (Figure 4e-f) and  
488 oxygen decreases (Figure 4g). This biological response can be attributed to cyclone-induced  
489 Ekman pumping upwelling and high subsurface vertical mixing. Enhanced nutrient availability  
490 at the subsurface layer can persist into the mixed layer, allowing for sufficient sunlight, and  
491 together with elevated oxygen concentrations (associated with surface cooling), may foster  
492 increased surface Chl-a and phytoplankton biomass. Signs of this can be seen in the MHW  
493 region, where higher Chl-a concentrations reach the surface. But, unlike previous results  
494 (Jangir et al., 2026), medicane Daniel only shows an increase in Chl-a at the surface in the  
495 MHW region.

496  
497 Profiles of temperature and Chl-a at the maximum cyclone intensity (Max-CI) location and  
498 time (Figure 4h-i) reveal general cooling after the passage of the cyclone. The deep chlorophyll  
499 maximum (DCM) was located far below the mixed layer depth, at around 140m depth. The  
500 subsurface crossings between the profiles and the relatively stationary location of the DCM in  
501 Figure 4i indicate that out of the two processes mentioned above, namely cyclone-induced  
502 upwelling and high subsurface vertical mixing, only cyclone-induced subsurface mixing can  
503 explain the change. Subsurface mixing mechanism is typically much slower than turbulence in  
504 the mixed layer, but under storm conditions may become comparable. The gradual subsurface  
505 increase in Chl-a, as opposed to the vertical line observed in the mixed layer, indicates weaker  
506 but comparable turbulence below the mixed layer.

507  
508 Figure 4i shows the change in subsurface profiles at the time and location of Max-CI, situated  
509 on the periphery of a WCE. To further investigate the underlying mechanisms and compare the  
510 medicane's impact on both WCEs and CCEs, vertical cross-sections across the main center of  
511 the WCE and adjacent CCE region were analyzed during the pre-storm, during storm, and post-  
512 storm phases (Figure 5). These cross-sections reveal notable eddy-dependent subsurface  
513 changes associated with the passage of the medicane. As expected, during and after the passage  
514 of the storm, significant surface cooling is observed in Figure 5 (panels b-d and h-i). In addition  
515 to the cooling observed within the mixed layer, three distinct circular-like cooling patterns are  
516 evident immediately beneath it. These may indicate a secondary circulation starting at the deep  
517 subsurface (below 200m), which transfers deep cold water to the layers below the mixed layer.  
518 In this case, the two patterns on the right indicate an upwelling cell at the ~~warm-core eddy~~WCE  
519 boundaries (green arrows in Figure 5i) and another at the ~~cold-core eddy~~CCE center (purple

520 arrow in Figure 5i). These circulation cells also create the dipole pattern in the Chl-a inside the  
521 WCE and the CCE (Figure 5, panels e-g and j-k).

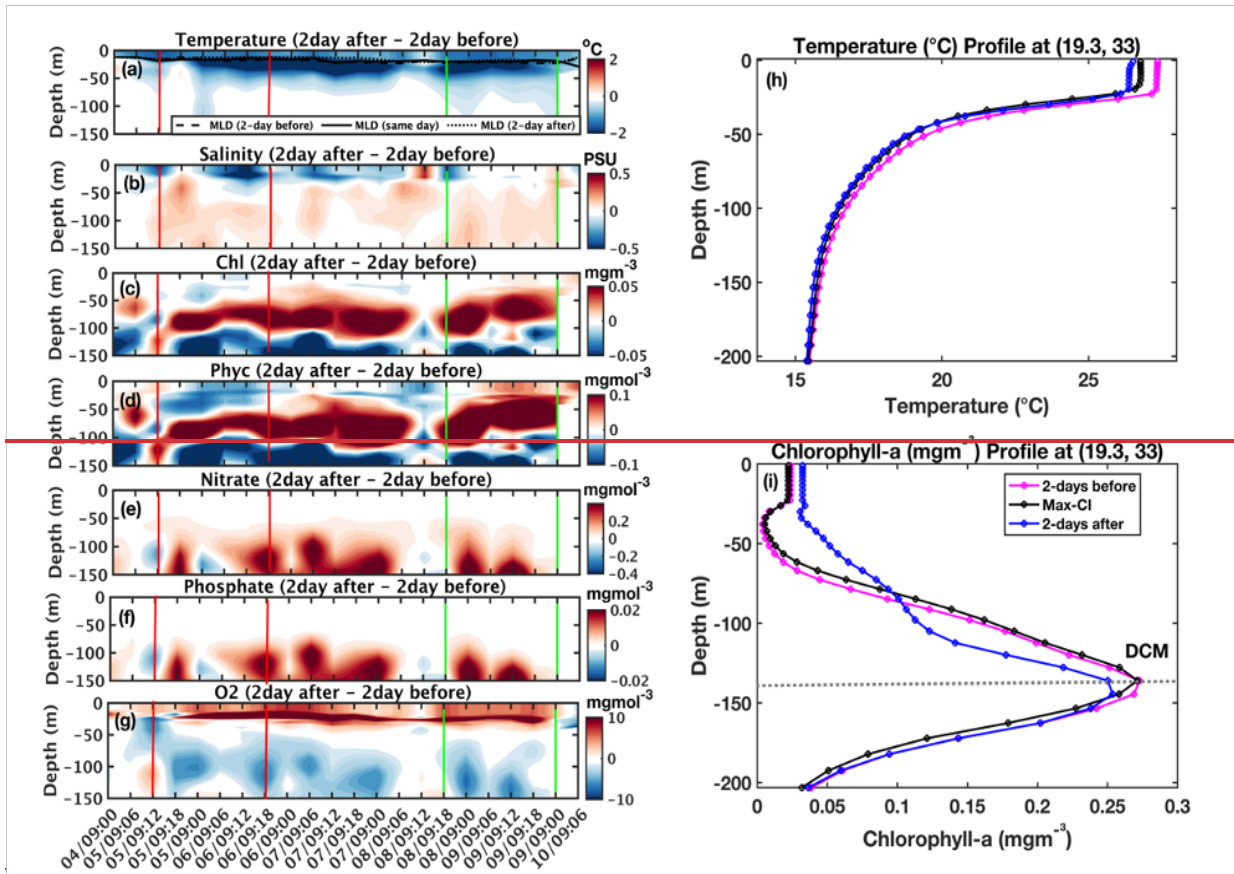
522

523 To explore the dynamical mechanisms, Figure 6 shows vertical profiles from 1 to 15 September  
524 2023 of Chl-a at two locations along the same line as in Figure 5a, one inside the CCE (panel  
525 a) and the other inside the WCE (panel b). Before the arrival of the medicane (1-5 September),  
526 the DCM within the CCE was shallower than in the WCE, consistent with the typical vertical  
527 structure of these eddies. The DCM in both eddies remains relatively stable until the cyclone  
528 approaches the region. As the medicane approaches the eddies, it intensifies the CCE while  
529 diminishing the WCE, which, as expected from theory (e.g., [Klein & Lapeyre, 2009](#)), supports  
530 eddy-induced upwelling. Indeed, during the storm, the DCM is lifted upward in both cases  
531 from 5 to 9 September. Yet, the DCM inside the WCE is exhibited significantly greater  
532 shoaling than inside the CCE (~ 40m in the WCE relative to ~ 15m in the CCE). The more  
533 pronounced response in the WCE likely stems from lower thermal stratification and higher  
534 surface wind stress curl that contribute to cyclone-induced Ekman pumping upwelling. Only a  
535 few days later, the DCM inside the WCE partially starts to restore its pre-storm condition. The  
536 DCM inside the CCE quickly drops back down and even overshoots its depth relative to pre-  
537 storm conditions, which can be explained by its stronger stratification and resulting buoyancy  
538 restoring force. In addition, we found that cyclone-induced upwelling alone cannot explain the  
539 DCM increase in both the WCE and CCE (Figure 6c), which indicates an increase of about 10-  
540 15 meters during the medicane influence (5-9 September). Therefore, we conclude that the  
541 upwelling may have also been influenced by isopycnal adjustment triggered by the medicane.

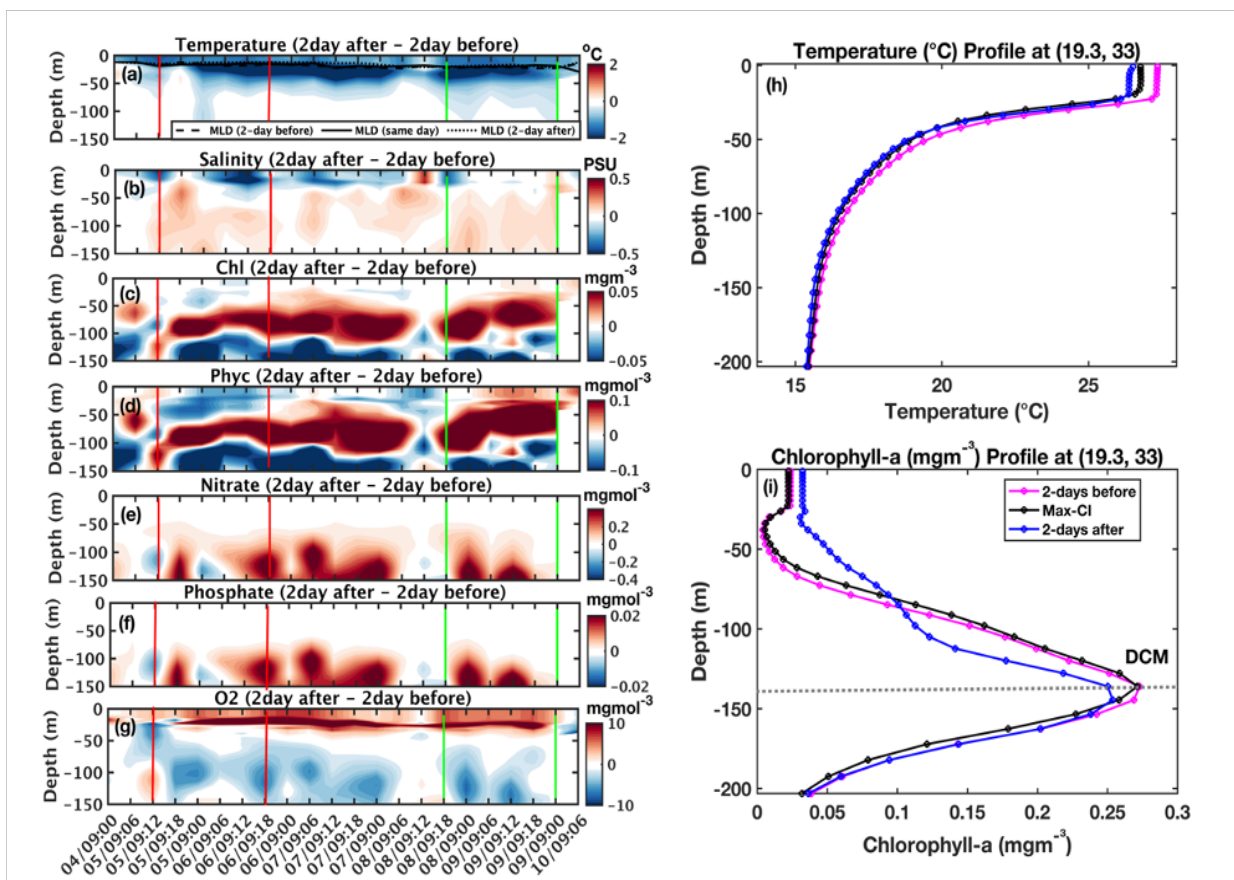
542

543 Subsurface mixing similar to what was shown under the medicane at Max-CI (Figure 4i), seems  
544 to play a role also here. This role can be indicated by the crossing of the Chl-a profiles during  
545 the storm (5-9 September) with the profiles after the storm (10-15 September) between MLD  
546 (~ -20m) and the DCM (~ -130m). However, here, it seems to complement upwelling and to  
547 play a more important role at the WCE (as expected, since in general wind stress is higher  
548 above WCEs). Also, satellite-based surface observations (Figure 6d) indicate higher Chl-a  
549 above the WCE region, which may be explained by the closer-to-the-surface DCM and stronger  
550 cyclone-induced upwelling and vertical mixing.

551

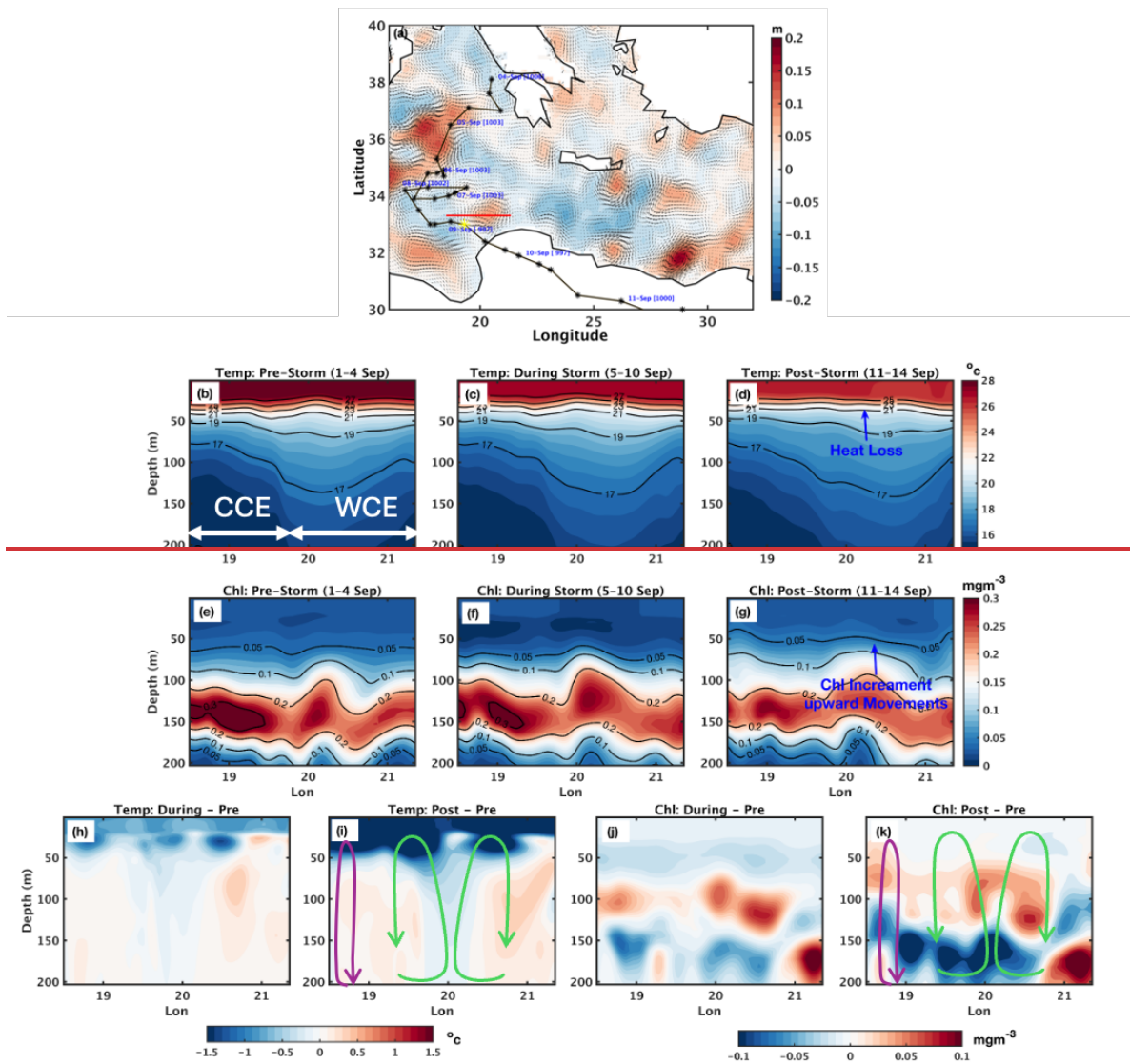


552

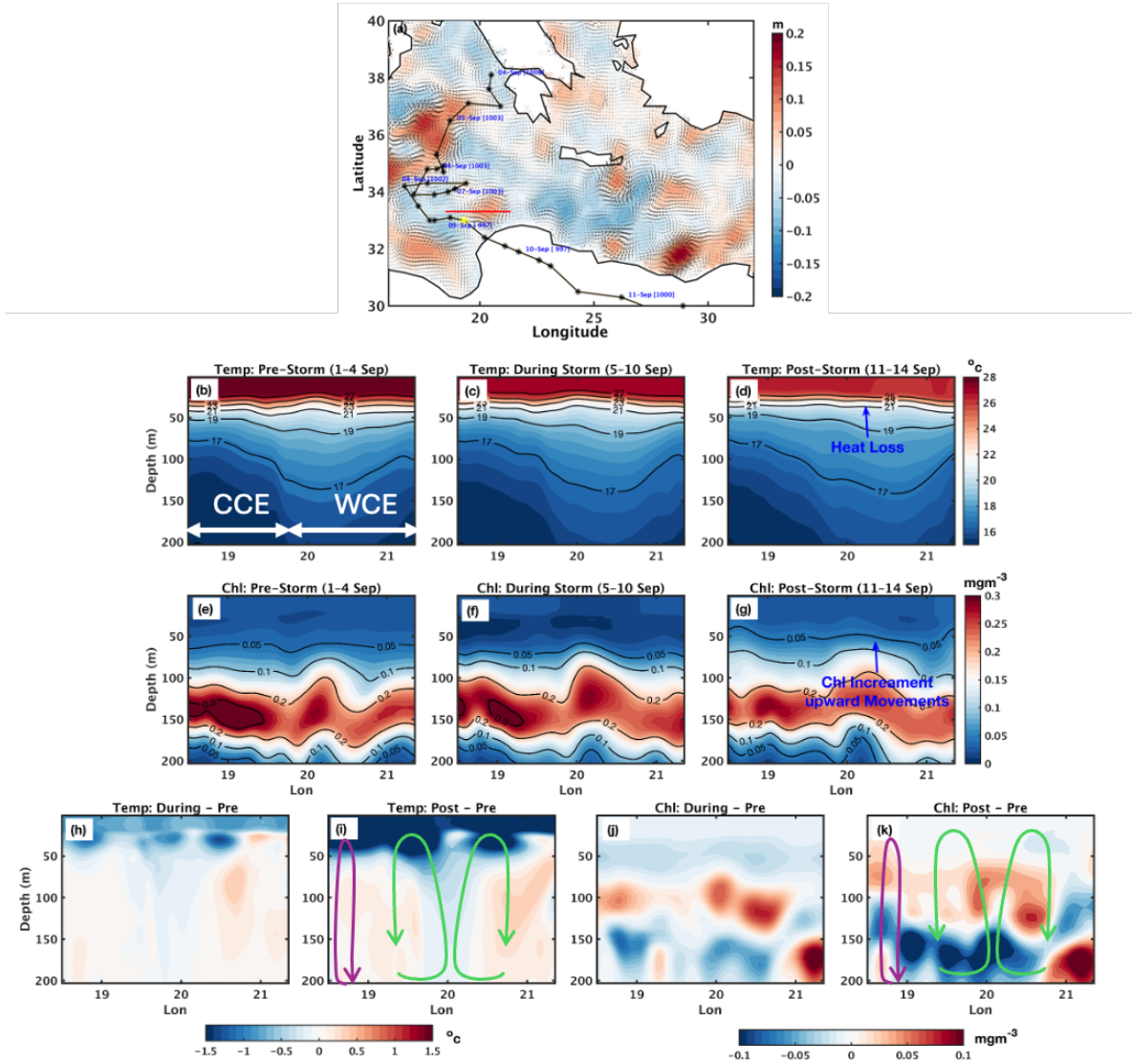


553

554 Figure 4: Profiles of physical (a-d) and biogeochemical (e-g) variables along the track of  
 555 medicane Daniel. The left panels show the difference between two days after and two days  
 556 before the event. Red and green vertical lines in panels (a-g) delineate the location of the warm-  
 557 core eddy (WCE) and marine ~~heatwave~~ heatwave (MHW) along the track, respectively. The  
 558 black line in the temperature profile indicates the mixed layer depth.  
 559



560



561

562 *Figure 5: (a) Sea level anomaly with a red line indicating the section across the second warm-*  
 563 *core eddy (WCE) used in subsequent panels. (b-d) Temperature profiles and isotherms before,*  
 564 *during, and after the medicane along this section. (e-g) Chlorophyll-a profiles before,*  
 565 *and after the medicane along the same section. (h-i) Temperature differences (during-storm*  
 566 *minus pre-storm, and post-storm minus pre-storm). (j-k) Same as (h-i), but for Chlorophyll-a.*  
 567 *Green arrows denote the location of a secondary circulation cell, and the purple arrow*  
 568 *indicates subsurface mixing.*

569

570

571

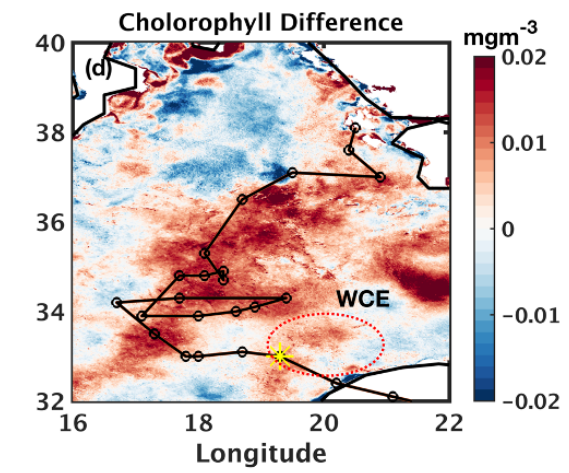
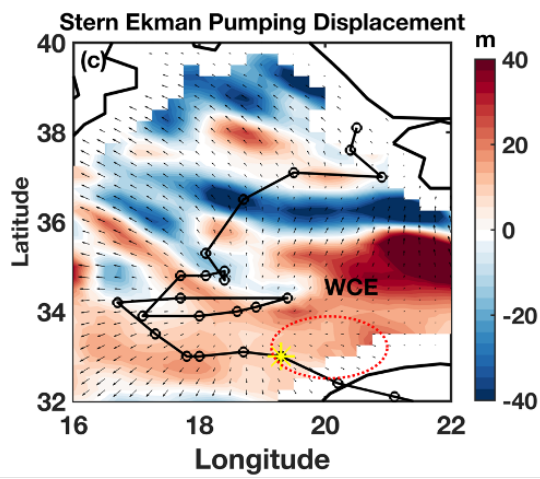
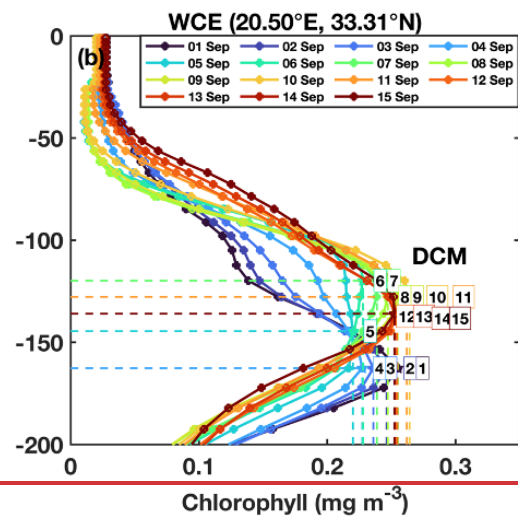
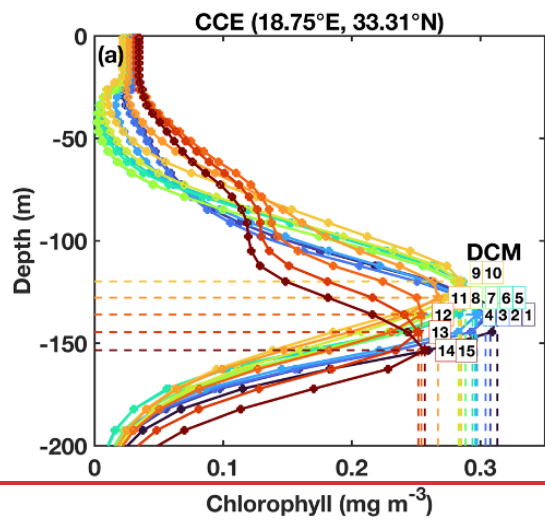
572

573

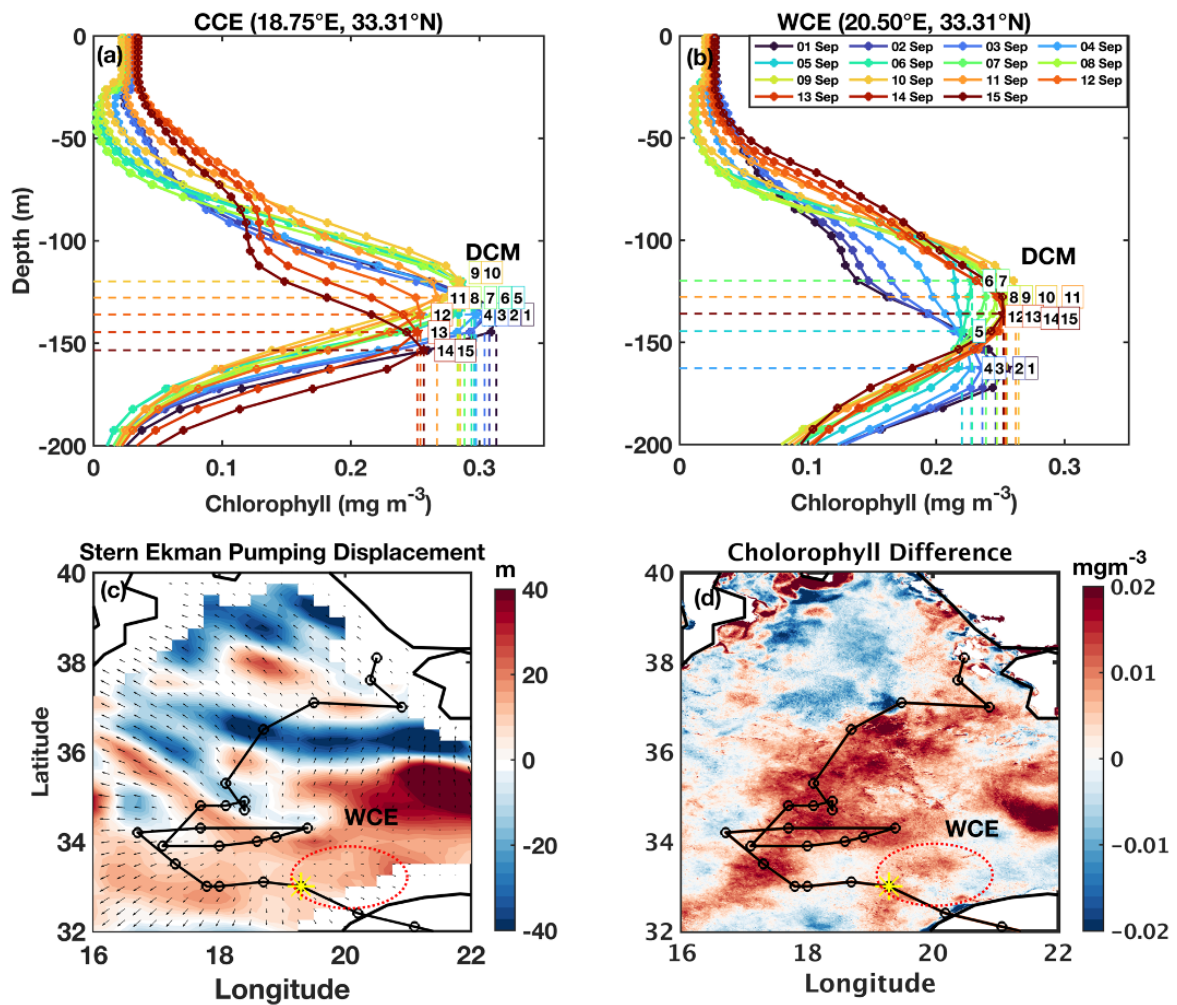
574

575

576



577



578

579

580 *Figure 6: Chlorophyll-a profiles from 1 to 15 September 2023 at the cold-core eddy (CCE; a)*  
 581 *and warm-core eddy (WCE; b) locations. (c) Cumulative Ekman pumping displacement for 5–*  
 582 *9 September 2023, with arrows indicating the transport vector during the cyclone. (d) Satellite*  
 583 *chlorophyll-a (2 km spatial resolution) before and after medicane Daniel. The red dotted*  
 584 *ellipse indicates the location of the ~~warm-core eddy~~WCE, and the yellow star denotes the*  
 585 *location of maximum cyclone intensity (Max-CI).*

586

### 587 5. Conclusions

588 This case study provides comprehensive insights into the intensification and impacts of  
 589 medicane Daniel, which developed over the Mediterranean Sea in September 2023. The  
 590 findings show the significant role of oceanic and atmospheric variables in cyclone  
 591 intensification, particularly the presence of WCE and MHW (Figure 7). These oceanic features  
 592 reduced the negative feedback loop between cyclone intensity and SST, allowing the cyclone  
 593 to maintain and even increase its intensity. This study also highlighted the importance of OHC

594 in providing the energy necessary for cyclone intensification, with approximately 120 KJ/cm<sup>2</sup>  
595 of heat available at the intensification location over the WCE and MHW. Additionally, the  
596 convergence of moisture at the locations of the WCE and MHW, combined with the elevated  
597 total water column, contributed to the heavy precipitation observed in the coastal areas in  
598 Libya.

599

600 This study highlights the critical role of high-resolution SWOT data in advancing our  
601 understanding of air-sea interaction processes. While CMEMS data, with its coarser spatial  
602 resolution, suggests the presence of a weak eddy near the cyclone intensification region,  
603 SWOT's finer 2 km resolution reveals a high-intensity WCE precisely aligned with the  
604 cyclone's path. This enhanced detection capability provides a more accurate illustration of eddy  
605 characteristics and their influence on cyclone dynamics. Furthermore, satellite-derived Chl-a  
606 data indicate an enhanced bloom over the WCE location, supported by positive Ekman  
607 pumping values. These high values indicate cyclone-induced upward movement of water from  
608 deeper layers to the surface, bringing cold, nutrient-rich water to the surface, and boosting  
609 ocean productivity.

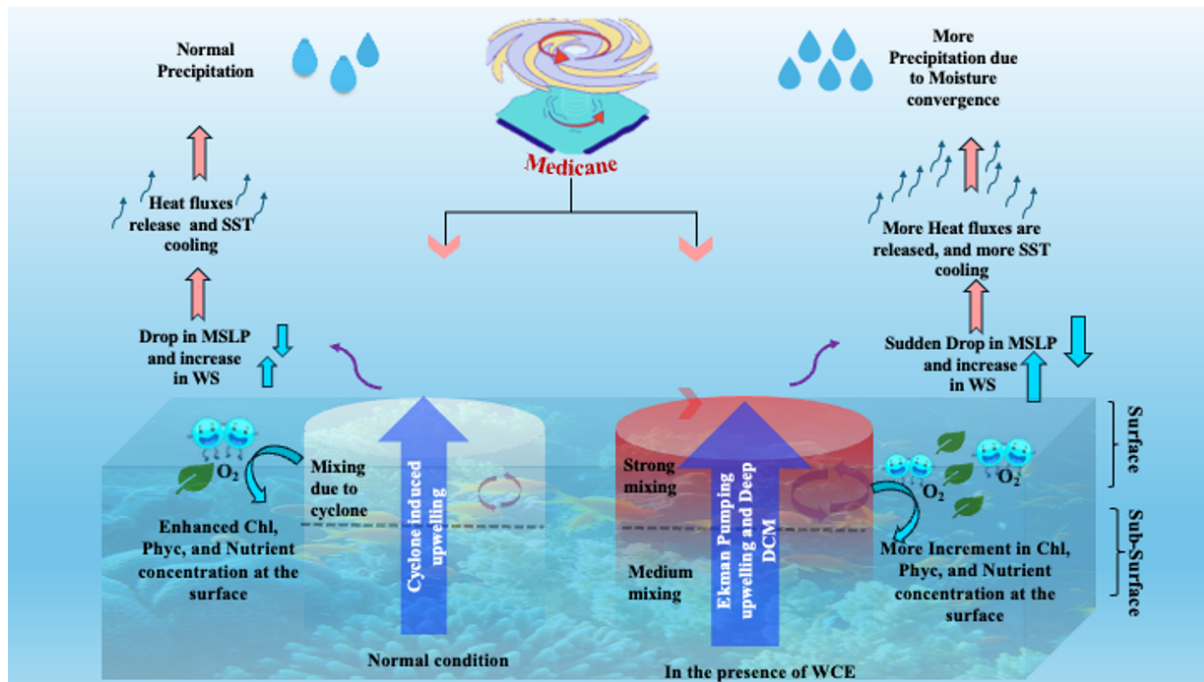
610

611 Subsurface profiles of physical and biogeochemical properties show a notable temperature  
612 decrease above the mixed layer depth, particularly over the WCE and MHW regions. The  
613 passage of the cyclone triggers vertical mixing, leading to an increase in surface nutrient  
614 concentrations. Combined with sufficient sunlight in the euphotic zone, this promotes a surge  
615 in surface Chl-a and phytoplankton productivity. Cross-sectional analysis further reinforces  
616 these findings: a clear upward shift in isotherms following the cyclone indicates heat loss and  
617 active upwelling over the WCE. Concurrently, the Chl-a sections display an upward  
618 displacement and intensification of Chl-a concentrations, confirming the strong  
619 biogeochemical response induced by the cyclone's passage over the WCE region.

620

621 In conclusion, the study of medicane Daniel emphasizes the need for a deeper understanding  
622 of both oceanic and atmospheric factors in predicting and mitigating the impacts of such  
623 cyclones in the Mediterranean region. The findings suggest that, similar to tropical cyclones in  
624 other ocean basins, medicanes are significantly influenced by the interplay of oceanic heat  
625 content, eddies, and atmospheric dynamics. These factors are responsible for the intensification  
626 of the cyclone and the destruction caused by the medicane.

627



629

630 *Figure 7: Schematic illustrating the process associated with cyclone intensification over warm-*  
 631 *core eddy and marine heatwave, and their impact on ocean biogeochemistry.*

632

633

#### 634 **Data Availability:**

635

636 Data can be Archived from the links below-

637 [https://doi.org/10.25423/cmcc/medsea\\_multiyear\\_bgc\\_006\\_008\\_medbfm3](https://doi.org/10.25423/cmcc/medsea_multiyear_bgc_006_008_medbfm3)

638 <https://doi.org/10.48670/moi-00298>

639 <https://zivipotty.hu/tcr.html>

640 [https://www.aviso.altimetry.fr/en/data/products/sea-surface-height-products/global/swot-13-](https://www.aviso.altimetry.fr/en/data/products/sea-surface-height-products/global/swot-13-ocean-products.html)  
 641 [ocean-products.html](https://www.aviso.altimetry.fr/en/data/products/sea-surface-height-products/global/swot-13-ocean-products.html)

642

#### 643 **Author Contributions:**

644 B.J. contributed to the conceptualization of the study, data curation, formal analysis, and  
 645 writing of the original draft.

646

647 E.S. served as the project investigator, contributed to conceptualization, provided resources  
 648 and software support, supervised the research, and contributed to review and editing, as well  
 649 as funding acquisition.

650

651 **Competing Interests:** The authors declare no conflict of interest.

652 **Acknowledgments:** The authors acknowledge the data-providing agencies (i.e., CMEMS,

653 AVISO) for providing data free of cost.

654 **Funding:** This research was supported by the Israel Science Foundation (Grant 2228/21).  
655

656 **References**

657 Ali, M. M., Jagadeesh, P. S. V. and Jain, S., 2007. Effects of eddies on Bay of Bengal cyclone intensity,  
658 *Eos Trans. AGU*, 88(8), 93–95, doi:[10.1029/2007EO080001](https://doi.org/10.1029/2007EO080001).

659  
660 Archer, M., Wang, J., Klein, P. *et al.*, 2025. Wide-swath satellite altimetry unveils global submesoscale  
661 ocean dynamics. *Nature* 640, 691–696. <https://doi.org/10.1038/s41586-025-08722-8>  
662

663 Avolio, E., Fanelli, C., Pisano, A., & Miglietta, M. M. 2024. Unveiling the relationship between  
664 Mediterranean tropical-like cyclones and rising Sea Surface Temperature. *Geophysical Research*  
665 *Letters*, 51, e2024GL109921. <https://doi.org/10.1029/2024GL109921>  
666

667 Bender, M. A., Ginis, I., and Kurihara, Y., 1993. Numerical simulations of tropical cyclone-ocean  
668 interaction with a high-resolution coupled model, *J. Geophys. Res.*, 98(D12), 23245–23263,  
669 doi:[10.1029/93JD02370](https://doi.org/10.1029/93JD02370).

670  
671 Berthon, J.-F., Zibordi, G., 2004. Bio-optical relationships for the northern Adriatic Sea. *Int. J. Remote*  
672 *Sens.*, 25, 1527-1532.

673  
674 Chen, Y., Pan, G., Mortimer, R., Zhao, H., 2022. Possible Mechanism of Phytoplankton Blooms at the  
675 Sea Surface after Tropical Cyclones. *Remote Sensing*. 14, 6207. doi: 10.3390/rs14246207  
676

677 Cherif, S., Doblas-Miranda, E., Lionello, P., Borrego, C., Giorgi, F., Iglesias, A., et al., 2020. Drivers of  
678 change. In *Climate and environmental change in the Mediterranean Basin—current situation and risks*  
679 *for the future* (pp. 59–128). First Mediterranean Assessment Report. Union for the Mediterranean, Plan  
680 Bleu, UNEP/MAP.

681  
682 Chowdhury, R. R., Prasanna Kumar, S., Narvekar, J., & Chakraborty, A., 2020. Back-to-back  
683 occurrence of tropical cyclones in the Arabian Sea during October–November 2015: Causes and  
684 responses. *Journal of Geophysical Research: Oceans*, 125, e2019JC015836. doi:  
685 [10.1029/e2019JC015836](https://doi.org/10.1029/e2019JC015836)  
686

687 Claud, C., Alhammoud, B., Funatsu, B. M., and Chaboureau, J.-P., 2010. Mediterranean hurricanes:  
688 large-scale environment and convective and precipitating areas from satellite microwave observations,  
689 *Nat. Hazards Earth Syst. Sci.*, 10, 2199–2213, <https://doi.org/10.5194/nhess-10-2199-2010>.

690  
691 Cressman, G. P., 1959. An operational objective analysis scheme. *Monthly Weather*  
692 *Review*, 87, 367–374. doi: [10.1175/1520-0493\(1959\)087<0367:aoas>2.0.co;2](https://doi.org/10.1175/1520-0493(1959)087<0367:aoas>2.0.co;2)  
693

694 Dutta, D., Mani, B. & Dash, M.K., 2019. Dynamic and thermodynamic upper-ocean response to the  
695 passage of Bay of Bengal cyclones ‘Phailin’ and ‘Hudhud’: a study using a coupled modelling system.  
696 *Environ Monit Assess* 191 (Suppl 3), 808.. <https://doi.org/10.1007/s10661-019-7704-9>.

697  
698 Emanuel, K., 2005. Genesis and maintenance of “Mediterranean hurricanes.” *Advances in Geosciences*,  
699 2, 217–220. <https://doi.org/10.5194/adgeo-2-217-2005>

700 Fita, L., Romero, R., Luque, A., Emanuel, K., and Ramis, C., (2007) Analysis of the environments of  
701 seven Mediterranean tropical-like storms using an axisymmetric, nonhydrostatic, cloud resolving  
702 model, *Nat. Hazards Earth Syst. Sci.*, 7, 41–56, <https://doi.org/10.5194/nhess-7-41-2007>.

703  
704 Flaounas, E., Raveh-Rubin, S., Wernli, H., Drobinski, P., and Bastin, S., (2015). The dynamical  
705 structure of intense Mediterranean cyclones, *Clim. Dynam.*, 44, 2411–2427,  
706 <https://doi.org/10.1007/s00382-014-2330-2>  
707  
708 Flaounas, E.; Davolio, S.; Raveh-Rubin, S.; Pantillon, F.; Miglietta, M.M.; Gaertner, M.A.; Hatzaki,  
709 M.; Homar, V.; Khodayar, S.; Korres, G.; et al., 2022. Mediterranean Cyclones: Current Knowledge  
710 and Open Questions on Dynamics, Prediction, Climatology and Impacts. *Weather Clim. Dyn.* 3, 173–  
711 208  
712  
713 Flaounas, E., Dafis, S., Davolio, S., Faranda, D., Ferrarin, C., Hartmuth, K., Hochman, A.,  
714 Koutroulis, A., Khodayar, S., Miglietta, M. M., Pantillon, F., Patlakas, P., Sprenger, M., and  
715 Thurnherr, I.: Dynamics, predictability, impacts and climate change considerations of the  
716 catastrophic Mediterranean Storm Daniel (2023), *Weather Clim. Dynam.*, 6, 1515–1538,  
717 <https://doi.org/10.5194/wcd-6-1515-2025>, 2025.  
718  
719 Flocas, H. A., 2000. Diagnostics of cyclogenesis over the Aegean sea using potential vorticity inversion,  
720 *Meteorol. Atmos. Phys.*, 73, 25–33, <https://doi.org/10.1007/s007030050061>  
721  
722 González-Alemán, J. J., Pascale, S., Gutierrez-Fernandez, J., Murakami, H., Gaertner, M. A., & Vecchi,  
723 G. A. (2019). Potential increase in hazard from Mediterranean hurricane activity with global warming.  
724 *Geophysical Research Letters*, 46, 1754–1764. <https://doi.org/10.1029/2018GL081253>  
725  
726 Hersbach, H., Bell, B., Berrisford, P., Hirahara, S., Horanyi, A., Muñoz-Sabater, J., et al., 2020. The  
727 Era5 global reanalysis. *Quarterly Journal of the Royal Meteorological Society*, 146, 1999–2049, doi:  
728 [10.1002/qj.3803](https://doi.org/10.1002/qj.3803).  
729  
730 Hérincs, D., 2023. *Tropical Storm Daniel: Mediterranean tropical cyclone report (7–10 September*  
731 *2023)*. Zivipotty.hu. [https://zivipotty.hu/2023\\_daniel.pdf](https://zivipotty.hu/2023_daniel.pdf)  
732  
733 Hobday, A. et al., 2016. A hierarchical approach to defining marine heatwaves. *Prog. Oceanogr.* 141,  
734 227–238.  
735  
736 Hobday, A.J., Oliver, E.C.J., Sen Gupta, A., Benthuisen, J.A., Burrows, M.T., Donat, M.G., Holbrook,  
737 N.J., Moore, P.J., Thomsen, M.S., Wernberg, T., and Smale, D.A., 2018. Categorizing and naming  
738 marine heatwaves. *Oceanography* 31(2):162–173, <https://doi.org/10.5670/oceanog.2018.205>.  
739  
740 Hochman, A., Scher, S., Quinting, J., Pinto, J. G., & Messori, G., 2021. A new view of heat wave  
741 dynamics and predictability over the eastern Mediterranean. *Earth System Dynamics*, 12(1), 133–149.  
742 <https://doi.org/10.5194/esd-12-133-2021>  
743  
744 IPCC., 2021. In V. Masson-Delmotte, P. Zhai, A. Pirani, S. L. Connors, C. Péan, et al. (Eds.), *Climate*  
745 *Change 2021: The Physical Science Basis. Contribution of Working Group I to the Sixth Assessment*

746 *Report of the Intergovernmental Panel on Climate Change*. Cambridge University Press.  
747 <https://doi.org/10.1017/9781009157896>  
748

749 Jangir B., Mishra A. K., Strobach, E., 2024. The interplay between medicanes and the Mediterranean  
750 Sea in the presence of sea surface temperature anomalies, *Atmospheric Research*, Volume 310, 107625,  
751 ISSN 0169-8095, <https://doi.org/10.1016/j.atmosres.2024.107625>.  
752

753 Jangir, B., Mishra, A. K., & Strobach, E., 2023. Effects of mesoscale eddies on the intensity of cyclones  
754 in the Mediterranean Sea. *Journal of Geophysical Research: Atmospheres*, 128, e2023JD038607, doi:  
755 [10.1029/2023JD038607](https://doi.org/10.1029/2023JD038607)  
756

757 Jangir, B., Swain, D., & Ghose, S., 2021. Influence of eddies and tropical cyclone heat potential on  
758 intensity changes of tropical cyclones in the North Indian Ocean. *Advances in Space Research*, 68(2),  
759 773–786, doi: [10.1016/j.asr.2020.01.011](https://doi.org/10.1016/j.asr.2020.01.011)  
760

761 Jangir, B., Reale, M., Menna, M., Mishra, A. K., Marellucci, R., Cossarini, G., et al. (2026). The  
762 response of the physical and biogeochemical marine environment to the passage of Mediterranean  
763 cyclones in the presence of eddies, gyres, and marine heat wave. *Journal of Geophysical Research:*  
764 *Oceans*, 131, e2025JC023151. <https://doi.org/10.1029/2025JC023151>  
765

766 Katsanos, D., Retalis, A., Kalogiros, J., Psiloglou, B. E., Roukounakis, N., & Anagnostou, M., 2024.  
767 Performance Evaluation of Satellite Precipitation Products During Extreme Events—The Case of the  
768 Medcane Daniel in Thessaly, Greece. *Remote Sensing*, 16(22), 4216.  
769 <https://doi.org/10.3390/rs16224216>  
770

771 Khodayar, S., Kushta, J., Catto, J. L., Dafis, S., Davolio, S., Ferrarin, C., et al., 2025. Mediterranean  
772 cyclones in a changing climate: A review on their socio-economic impacts. *Reviews of Geophysics*, 63,  
773 e2024RG000853. <https://doi.org/10.1029/2024RG000853>.  
774

775 Klein, P., and Lapeyre, G., 2009. The Oceanic Vertical Pump Induced by Mesoscale and Submesoscale  
776 Turbulence. *Annual Review of Marine Science*, 1(Volume 1, 2009):351–375, 2009. ISSN 1941-0611.  
777 doi:<https://doi.org/10.1146/annurev.marine.010908.163704>.  
778  
779

780 Kouroutzoglou, J., Flocas, H. A., Keay, K., Simmonds, I., and Hatzaki, M., 2011. Climatological  
781 aspects of explosive cyclones in the Mediterranean, *Int. J. Climatol.*, 31, 1785–1802,  
782 <https://doi.org/10.1002/joc.2203>.  
783

784 Latha, P. T., Rao, K.H., Nagamani, P.V., Amminedu, E., Choudhury, S.B., Dutt, C.B.S. and Dadhwal,  
785 V.K., 2015. Impact of Cyclone PHAILIN on Chlorophyll-a Concentration and Productivity in the Bay  
786 of Bengal. *International Journal of Geosciences*, 6, 473-480, doi: [10.4236/ijg.2015.65037](https://doi.org/10.4236/ijg.2015.65037).  
787

788 Law K., 2011. The Impact of Oceanic Heat Content on the Rapid Intensification of Atlantic Hurricanes,  
789 Chapter 17. In: Lupo, A., eds. *Recent Hurricane Research - Climate, Dynamics, and Societal Impacts*.  
790 Croatia : InTech: 331-354.  
791

792 Li, D., Chang, P., Ramachandran, S., Jing, Z., Zhang, Q., Kurian, J., Gopal, A., & Yang, H. (2021).  
793 Contribution of the Two Types of Ekman Pumping Induced Eddy Heat Flux to the Total Vertical Eddy

794 Heat Flux. *Geophysical Research Letters*, 48(9), e2021GL092982.  
795 <https://doi.org/10.1029/2021GL092982>.  
796  
797 Lin, I. I., Goni, G. J., Knaff, J. A., ZForebas, C., Ali, M. M.,2013. Ocean heat content for tropical  
798 cyclone intensity forecasting and its impact on storm surge, *Nat. Hazards*, 66, pp. 1481-1500,  
799 10.1007/s11069-012-0214-5  
800  
801 Liu, Y., Tang, D., Tang, S., Morozov, E., Liang, W., Sui, Y.,2020. A case study of Chlorophyll a  
802 response to tropical cyclone Wind Pump considering Kuroshio invasion and air-sea heat exchange.  
803 *Science of Total Environment*, 741:140290. doi: 10.1016/j.scitotenv.2020.140290. Epub 2020 Jun 18.  
804 PMID: 32603939.  
805  
806 Ma, Z.,2018. Examining the contribution of surface sensible heat flux induced sensible heating to  
807 tropical cyclone intensification from the balance dynamics theory. *Dynamics of Atmospheres and*  
808 *Oceans*, 84, 33–45. <https://doi.org/10.1016/j.dynatmoce.2018.09.001>  
809  
810 MedECC.,2020. Climate and environmental change in the Mediterranean Basin—Current situation and  
811 risks for the future. In W. Cramer, J. Guiot, & K. Marini (Eds.), *First Mediterranean assessment report*,  
812 Union for the Mediterranean, Plan Bleu (p. 632). UNEP/MAP.  
813  
814 Menna, M., Martellucci, R., Reale, M. *et al.*,2023 A case study of impacts of an extreme weather system  
815 on the Mediterranean Sea circulation features: Medicanes Apollo (2021). *Scientific Report*, 13, 3870, doi:  
816 [10.1038/s41598-023-29942-w](https://doi.org/10.1038/s41598-023-29942-w).  
817  
818 Miglietta, M.M.,Rotunno, R., 2019. Development Mechanisms for Mediterranean Tropical-like  
819 Cyclones (Medicanes). *Q. J. R. Meteorol. Soc.* 145, 1444–1460.  
820  
821 Mishra, A.K., Jangir, B. & Strobach, E., 2024. Influence of mesoscale sea-surface temperature  
822 structures on the Mediterranean cyclone Ianos in convection-permitting simulations: Contributions of  
823 surface warming and cold wakes. *Quarterly Journal of the Royal Meteorological Society*, 150(765),  
824 5146–5166. <https://doi.org/10.1002/qj.4862>  
825  
826 Morrow, R., et al.,2019. "Global observations of fine-scale ocean surface topography with the Surface  
827 Water and Ocean Topography (SWOT) mission." *Frontiers in Marine Science*, 6, 232.  
828 <https://doi.org/10.3389/fmars.2019.00232>.  
829  
830 Nicolaides, K. A., Michalelides, S. C., and Karacostas, T. (2006). Synoptic and dynamic characteristics  
831 of selected deep depressions over Cyprus, *Adv. Geosci.*, 7, 175–180, [https://doi.org/10.5194/adgeo-7-](https://doi.org/10.5194/adgeo-7-175-2006)  
832 [175-2006](https://doi.org/10.5194/adgeo-7-175-2006), 2006.  
833  
834 Normand, J.C.L., Heggy, E., 2024. Assessing flash flood erosion following storm Daniel in Libya. *Nat*  
835 *Commun* 15, 6493. <https://doi.org/10.1038/s41467-024-49699-8>  
836  
837 Oliver, E.C.J., Donat, M.G., Burrows, M.T. *et al.*, 2018. Longer and more frequent marine heatwaves  
838 over the past century. *Nat Commun* 9, 1324. <https://doi.org/10.1038/s41467-018-03732-9>  
839

840 Panegrossi, G., D’Adderio, L. P., Dafis, S., Rysman, J.-F., Casella, D., Dietrich, S., & Sanò, P., 2023.  
841 Warm Core and Deep Convection in Medicanes: A Passive Microwave-Based Investigation. *Remote*  
842 *Sensing*, 15(11), 2838. <https://doi.org/10.3390/rs15112838>  
843  
844 Pytharoulis, I., Kartsios, S., Tegoulas, I., Feidas, H., Miglietta, M. M., Matsangouras, I., & Karacostas,  
845 T.,2018. Sensitivity of a Mediterranean Tropical-Like Cyclone to Physical Parameterizations.  
846 *Atmosphere*, 9(11), 436. <https://doi.org/10.3390/atmos9110436>  
847  
848 Raveh-Rubin, S. and Flaounas, E., 2017. A dynamical link between deep Atlantic extratropical cyclones  
849 and intense Mediterranean cyclones. *Atmospheric Science Letters*, 18: 215-221.  
850 <https://doi.org/10.1002/asl.745>  
851  
852 Reale, M., Cabos, W., Cavicchia, L., Conte, D., Coppola, E., Flaounas, E., et al.,2022. Future  
853 projections of Mediterranean cyclone characteristics using the Med-CORDEX ensemble of coupled  
854 regional climate system models. *Climate Dynamics*, 58(9–10), 2501–2524.  
855 <https://doi.org/10.1007/s00382-021-06018-x>  
856  
857 Reynolds, R. W., Smith, T. M., Liu, C., Chelton, D. B., Casey, K. S., and Schlax, M. G., 2007. Daily  
858 High-Resolution-Blended Analyses for Sea Surface Temperature. *J. Climate*, 20, 5473–5496,  
859 <https://doi.org/10.1175/2007JCLI1824.1>.  
860  
861 Scardino, G., Kushabaha, A., Miglietta, M. M., Bonaldo, D., and Scicchitano, G.: When storms stir the  
862 Mediterranean depths: chlorophyll *a* response to Mediterranean cyclones, *Ocean Sci.*, 21, 2849–2872,  
863 <https://doi.org/10.5194/os-21-2849-2025>, 2025.  
864  
865 Scardino, G., Miglietta, M.M., Kushabaha, A. *et al.*,2024. Fingerprinting Mediterranean hurricanes  
866 using pre-event thermal drops in seawater temperature. *Sci Rep* 14, 8014.  
867 <https://doi.org/10.1038/s41598-024-58335-w>  
868  
869 Shang, X.-D., Zhu, H.-B., Chen, G.-Y., Xu, C., & Yang, Q.,2015. Research on cold core eddy change  
870 and phytoplankton bloom induced by typhoons: Case studies in the South China Sea. *Advances in*  
871 *Meteorology*, 1–19.doi: [10.1155/2015/340432](https://doi.org/10.1155/2015/340432).  
872  
873 Shang, X.-D., Zhu, H.-B., Chen, G.-Y., Xu, C., & Yang, Q.,2015. Research on cold core eddy change  
874 and phytoplankton bloom induced by typhoons: Case studies in the South China Sea. *Advances in*  
875 *Meteorology*, 1–19.doi: [10.1155/2015/340432](https://doi.org/10.1155/2015/340432).  
876  
877 Sharma, V., & Ali, M. M.,2014. Importance of ocean heat content for cyclone studies. *Journal of*  
878 *Climatology & Weather Forecasting*, 2(1), 1–6. [https://www.longdom.org/open-access/importance-of-](https://www.longdom.org/open-access/importance-of-ocean-heat-content-for-cyclone-studies-9577.html)  
879 [ocean-heat-content-for-cyclone-studies-9577.html](https://www.longdom.org/open-access/importance-of-ocean-heat-content-for-cyclone-studies-9577.html)  
880  
881 Strobach, E., Mishra, A.K., Jangir, B. *et al.*, 2024. Intensification of a rain system imparted by  
882 Mediterranean mesoscale eddies. *Sci Rep* 14, 26810. <https://doi.org/10.1038/s41598-024-76767-2>  
883  
884 Stern, M., 1965, Interaction of a uniform wind stress with a geostrophic vortex, *Deep Sea Res. Oceanogr.*  
885 *Abstr.*, 12(3), 355–367.  
886

887 Sun, M., Tian, F., Liu, Y., & Chen, G., 2017. An Improved Automatic Algorithm for Global Eddy  
888 Tracking Using Satellite Altimeter Data. *Remote Sensing*, 9(3), 206. <https://doi.org/10.3390/rs9030206>  
889

890 Trigo, I. F., Bigg, G. R., and Davies, T. D., 2002. Climatology of cyclogenesis mechanisms in the  
891 Mediterranean, *Mon. Weather Rev.*, 130, 549–569.  
892

893 Vidya, P. J., Balaji, M., Mani Murali, R., 2021. Cyclone Hudhud-eddy induced phytoplankton bloom  
894 in the northern Bay of Bengal using a coupled model, *Progress in Oceanography*, Volume 197, 102631,  
895 ISSN 0079-6611, <https://doi.org/10.1016/j.pocean.2021.102631>.  
896

897 Volpe, G., Buongiorno Nardelli, B., Colella, S., Pisano, A. and Santoleri, R.,2018. An Operational  
898 Interpolated Ocean Colour Product in the Mediterranean Sea, in *New Frontiers in Operational*  
899 *Oceanography*, edited by E. P. Chassignet, A. Pascual, J. Tintorè, and J. Verron, pp. 227–244.  
900

901 Volpe, G., Colella, S., Brando, V. E., Forneris, V., Padula, F. L., Cicco, A. D., & Santoleri, R.,2019.  
902 Mediterranean Ocean Colour Level 3 operational multi-sensor processing. *Ocean Science*, 15(1), 127-  
903 146.  
904

905 Wada, A., & Usui, N.,2007. Impact of tropical cyclone heat potential on tropical cyclone intensity in  
906 the western North Pacific Ocean. *Journal of Oceanography*, 63(3), 505–516.  
907 <https://doi.org/10.1007/s10872-007-0039-0>  
908

909 Wada, A., Usui, N., 2007. Importance of tropical cyclone heat potential for tropical cyclone intensity  
910 and intensification in the Western North Pacific. *J Oceanogr* 63, 427–447.  
911 <https://doi.org/10.1007/s10872-007-0039-0>  
912

913 Tranchant, Y. T., Legresy, B., Foppert, A., et al., 2025. SWOT reveals fine-scale balanced motions and  
914 dispersion properties in the Antarctic Circumpolar Current. *ESS Open Archive* .  
915 [10.22541/essoar.173655552.25945463/v1](https://doi.org/10.22541/essoar.173655552.25945463/v1)  
916

917 Zhang, Z., & Qiu, B.,2020. Surface Chlorophyll Enhancement in Mesoscale Eddies by Submesoscale  
918 Spiral Bands. *Geophysical Research Letters*, 47, e2020GL088820.  
919 <https://doi.org/10.1029/2020GL088820>  
920

921 Zhao et al., 2019. A MATLAB toolbox to detect and analyze marine heatwaves. *Journal of Open Source*  
922 *Software*, 4(33), 1124, <https://doi.org/10.21105/joss.01124>  
923

924 Zittis, G., Almazroui, M., Alpert, P., Ciais, P., Cramer, W., Dahdal, Y., et al.,2022. Climate change and  
925 weather extremes in the Eastern Mediterranean and Middle East. *Reviews of Geophysics*, 60(3),  
926 e2021RG000762. <https://doi.org/10.1029/2021RG000762>.  
927  
928  
929